Monthly Notices
of the
ROYAL ASTRONOMICAL SOCIETY

MNRAS **465,** 1720–1740 (2017)
Advance Access publication 2016 October 5

doi:10.1093/mnras/stw2522

How multiple supernovae overlap to form superbubbles

Naveen Yadav,[1⋆] Dipanjan Mukherjee,[2] Prateek Sharma[1⋆] and Biman B. Nath[3]

[1]*Department of Physics & Joint Astronomy Programme, Indian Institute of Science, Bangalore 560012, India*
[2]*Research School of Astronomy & Astrophysics, Mount Stromlo Observatory, ACT 2611, Australia*
[3]*Raman Research Institute, Sadashiva Nagar, Bangalore 560080, India*

Accepted 2016 September 30. Received 2016 September 29; in original form 2016 March 2

ABSTRACT

We explore the formation of superbubbles through energy deposition by multiple supernovae (SNe) in a uniform medium. We use the total energy conserving, 3D hydrodynamic simulations to study how SNe correlated in space and time create superbubbles. While isolated SNe fizzle out completely by ∼1 Myr due to radiative losses, for a realistic cluster size it is likely that subsequent SNe go off within the hot/dilute bubble and sustain the shock till the cluster lifetime. For realistic cluster sizes, we find that the bubble remains overpressured only if, for a given n_{g0}, $N_{\rm OB}$ is sufficiently large. While most of the input energy is still lost radiatively, superbubbles can retain up to ∼5–10 per cent of the input energy in the form of kinetic+thermal energy till 10 Myr for interstellar medium density $n_{g0} \approx 1$ cm^{-3}. We find that the mechanical efficiency decreases for higher densities ($\eta_{\rm mech} \propto n_{g0}^{-2/3}$). We compare the radii and velocities of simulated supershells with observations and the classical adiabatic model. Our simulations show that the superbubbles retain only $\lesssim 10$ per cent of the injected energy, thereby explaining the observed smaller size and slower expansion of supershells. We also confirm that a sufficiently large ($\gtrsim 10^4$) number of SNe are required to go off in order to create a steady wind with a stable termination shock within the superbubble. We show that the mechanical efficiency increases with increasing resolution, and that explicit diffusion is required to obtain converged results.

Key words: hydrodynamics – methods: numerical – ISM: bubbles.

1 INTRODUCTION

H I holes, shells, rings, expanding cavities, galactic chimneys, and filaments are ubiquitous structures which are embedded in the large-scale gas distribution of a galaxy. Heiles (1979) identified large cavities in the local interstellar medium (ISM) with energy requirement of $\gtrsim 3 \times 10^{52}$ erg as supershells. Our Solar system is itself embedded in such a cavity (radius ∼100 pc) filled with hot (∼10^6 K) and tenuous ($n \sim 5 \times 10^{-3}$ cm^{-3}) plasma (Sanders et al. 1977; McCammon et al. 1983) known as the local hot bubble (LHB).

When the size of a superbubble becomes comparable to the galactic H I scale height, it may break out of the galactic disc if the shell is sufficiently fast (e.g. Mac Low & McCray 1988; Roy et al. 2013) and inject energy and metals into the galactic halo. The widely accepted model of galaxy-scale superwinds involves injection of mechanical energy by massive stars in the form of radiation ($L_\star$), stellar winds ($L_{\rm w}$), and supernova (SN) explosions ($E_{\rm SN} \sim 10^{51}$ erg). Clearly, such large cavities cannot be created by either the wind from a single massive star or the SN explosion of a single star. Further, it is known from observations of O-type stars in the Galaxy that ∼70 per cent of them are associated with clusters and OB associations and a very small fraction of the known O-stars are isolated (Chu & Gruendl 2008). Out of the remaining 30 per cent, more than one-third are runaway stars which have been ejected in close gravitational encounters (Gies 1987). Hence, the most plausible mechanism for the formation of large superbubbles is quasi-continuous energy injection from multiple stars. The expanding shells of each individual star/SN merge to form a large-scale bubble known as a superbubble.

Pikel'Ner (1968) and Avedisova (1972) studied the interaction of a strong stellar wind with the ISM. The circumstellar shell enters the snowplow phase when the radiative cooling time-scale for the swept gas becomes equal to the dynamical age of the shell. Weaver et al. (1977) calculated the detailed structure for interaction of a strong stellar wind with the ISM. Castor, McCray & Weaver (1975) obtained a solution for the case of continuous energy injection (at a point) inside a homogeneous medium by a stellar wind ($L_{\rm w} = \dot{M} v_{\rm w}^2/2$) in the absence of radiative energy losses and found the presence of a transition region dominated by thermal conduction between the cold outer layer of the shell (shocked ISM) and the hot inner layer of the shell (shocked stellar wind). Weaver et al. (1977) analytically calculated detailed structure of the bubble in various phases of evolution, including the effects of radiative cooling. McCray & Kafatos (1987) highlighted that the stellar initial mass function and stellar ages are such that the impact of mechanical

⋆ E-mail: naveen.phys@gmail.com (NY); prateek@physics.iisc.ernet.in (PS)

energy input from SNe within a star cluster can be well modelled as a constant luminosity-driven superbubble.

Chevalier & Clegg (1985, hereafter CC85) obtained the steady wind solution driven by a constant rate of mass and thermal energy injection within a small spherical volume. Their solution is subsonic within the injection radius, and beyond that reaches a constant supersonic speed. They applied their wind solution to understand the observations of the galactic outflow in M82. Tomisaka, Habe & Ikeuchi (1981) performed 1D calculations in a medium with constant particle density. In their calculations, all explosions occur at the same point in space sequentially inside the cavity created by previous SNe. Vasiliev, Nath & Shchekinov (2015) have recently carried out 3D simulations in which SNe are uniformly distributed throughout the simulation box. Durier & Dalla Vecchia (2012) studied the concordance of SNe feedback methods based on thermal energy deposition and kinetic energy deposition. Sharma et al. (2014) (hereafter SRNS14) show that the isolated SN, in typical ISM conditions, loses almost all their mechanical energy by radiative losses by $\lesssim$0.1 Myr, whereas a sequence of explosions occurring inside the cavity blown by previous SNe can retain up to ∼40 per cent of the injected mechanical energy for few tens of Myr (of the order of the galactic dynamical time ∼50 Myr). Krause et al. (2013, 2014) have studied the evolution of interacting interstellar bubbles of three massive stars in a uniform medium. Their key finding is that a larger fraction of energy is retained in the ISM for more closely packed stars. The hot bubble mostly emits in soft X-rays below 1.0 keV.

Understanding the impact of massive stars, via their radiation, winds, and SNe, on the ISM is essential for star and galaxy formation. Observed star formation is inefficient both locally on molecular cloud scales (e.g. Krumholz & Tan 2007) and globally on galactic scales (e.g. Kauffmann et al. 2003). Supersonic turbulence, magnetic fields, radiative photoionization and jet feedback from massive stars, etc., are invoked to explain the inefficiency of star formation on molecular cloud scales (Krumholz et al. 2014 and references therein). Because of several complex processes involved, there is no consensus on the relative contribution of these different mechanisms acting on molecular cloud scales. The situation is slightly better on galactic scales ($\gtrsim$ 1 kpc) at which thermal SN feedback seems to be the dominant mechanism for regulating star formation (e.g. Strickland et al. 2004; De Avillez & Breitschwerdt 2005; Joung & Mac Low 2006; Creasey, Theuns & Bower 2013; Hennebelle & Iffrig 2014; Li et al. 2015).

It is well recognized that isolated SNe suffer catastrophic cooling losses in high-density clouds in which they are born (e.g. Thornton et al. 1998). In this case, almost all of the injected energy is lost rather than coupling to the ISM, especially over global dynamical timescales (∼10s of Myr). Even when SNe coalesce before each of them suffer radiative losses (i.e. if the SN rate density is high enough), they only retain ∼10 per cent of the injected energy (Sharma et al. 2012). Even such a small efficiency of mechanical energy coupling to the ISM appears more than enough to significantly suppress star formation on global scales for Milky Way and lower mass galaxies (e.g. Efstathiou 2000; red dot–dashed line in fig. 4 of Sharma et al. 2012).

Shocks generated by supersonic turbulence (expected within the dense shell) enhance density perturbations and gravitational instability *locally* (e.g. McCray & Kafatos 1987), but turbulence and magnetic fields in the dense shell, in all likelihood, prevent efficient *global* star formation (e.g. Stone & Norman 1992; Mac Low & Klessen 2004). Since turbulence can only be faithfully captured in 3D, it is necessary to study the ISM using 3D simulations.

The problem of star–ISM interaction involves complex chemical, ionization/recombination, thermal, and dynamical processes, and it is necessary to begin with understanding the most important processes in some detail. Multi-physics simulations (including gravity, chemistry, photoelectric heating, molecular physics, and SNe feedback) of ISM have been done by many authors (e.g. Gatto et al. 2015; Martizzi, Faucher-Giguère & Quataert 2015; Walch & Naab 2015; Walch et al. 2015). In this paper, we ignore all these processes except for idealized dynamical and thermal processes associated with SNe resulting from the death of massive stars. We also ignore magnetic fields and thermal conduction, which can greatly modify the structures with large temperature gradients (e.g. fig. 9 of SRNS14). We only consider the hot and warm phases of the ISM by turning off cooling below 10^4 K, corresponding to the thermally stable warm neutral medium (WNM) of the ISM. We do not consider the denser cold neutral phase because: (i) the stable cold phase exists globally only for a large enough ISM pressure, and hence is unlikely to be present in substantial amount in galaxies less massive than Milky Way (Wolfire et al. 1995); (ii) our focus is on feedback at scales larger than molecular clouds, and we assume that a good fraction of SN energy is able to leak out (aided by low-density channels formed due to stellar winds and radiation) into the more uniformly spread and geometrically thicker warm neutral disc. Thus, this paper is a generalization of 1D simulations of SRNS14, with a realistic spatial distribution of SNe in 3D. Unlike that work, we also use a total energy conserving code so that the value of mechanical efficiency is more accurate.

In this paper, we study the formation of superbubbles using idealized 3D hydrodynamic numerical simulations of SNe exploding in an initially homogeneous, isotropic ISM. Ours are among the highest resolution uniform-grid 3D simulations of their kind. In Section 2, we describe the physical setup and numerical simulations. In Section 3.1, we describe the key results from our simulations. Section 4 discusses analytic estimates and implications of our work. In Section 5, we conclude.

2 PHYSICAL SETUP

We choose an idealized physical setup of a uniform ISM at 10^4 K, corresponding to the WNM maintained in thermal balance by photoelectric/photoionization and cosmic ray heating (Wolfire et al. 1995). The Milky Way Giant Molecular Clouds (GMCs) have gas (H_2) densities ranging from 10 to 1000 cm^{-3} and mean size around ≈10–20 pc, as shown in Roman-Duval et al. (2010). Our scales of interest are much bigger ($\gtrsim$100 pc), corresponding to the WNM. Thermal energy is injected by SNe going off at random locations inside a spherical 'star cluster' and plasma is allowed to cool due to free–free and line emission till 10^4 K. The key aim is to study the dynamics and thermodynamics of SNe coalescing in the WNM and to study the conditions for the formation of overpressured superbubbles.

2.1 Simulation setup

We solve the hydrodynamic equations for the evolution of density, velocity, and pressure in 3D Cartesian coordinates using the static grid version of the finite volume, conservative, Godunov Eulerian code PLUTO (Mignone et al. 2007). The mass and energy injected due to SNe are added as source terms. The grid spacing is taken to be uniform in x, y, and z directions. We numerically solve the

following equations:

$$\frac{\partial \rho}{\partial t} + \boldsymbol{v} \cdot \nabla \rho + \rho \nabla \cdot \boldsymbol{v} = \dot{\rho}_{\rm SN}(t, \boldsymbol{x}), \quad (1)$$

$$\frac{\partial \boldsymbol{v}}{\partial t} + \boldsymbol{v} \cdot \nabla \boldsymbol{v} + \frac{1}{\rho} \nabla p = 0, \quad (2)$$

$$\frac{\partial p}{\partial t} + \boldsymbol{v} \cdot \nabla p + \rho c_s^2 \nabla \cdot \boldsymbol{v} = (\gamma - 1)\{\dot{e}_{\rm SN}(t, \boldsymbol{x}) - \dot{e}_{\rm rad}(t, \boldsymbol{x})\}, \quad (3)$$

where symbols have their usual meanings, $c_s = (\gamma p/\rho)^{1/2}$ is the sound speed, $\dot{\rho}_{\rm SN}$ is the mass density source term, $\dot{e}_{\rm SN}$ is the thermal energy source term mimicking SN feedback (see Section. 2.2), and $\dot{e}_{\rm rad} \equiv n_{\rm e} n_{\rm i} \Lambda[T]$ ($n_{\rm e}$ is electron number density, $n_{\rm i}$ is ion number density, and $\Lambda[T]$ is the temperature-dependent cooling function) is the rate of energy loss per unit volume due to radiative cooling. We use the ideal gas equation

$$\rho \epsilon = \frac{p}{(\gamma - 1)} \quad (4)$$

with $\gamma = 5/3$ (ϵ is internal energy per unit mass).

PLUTO solves the system of conservation laws, which can be written as

$$\frac{\partial \boldsymbol{u}}{\partial t} = -\nabla \cdot \boldsymbol{\Pi} + \boldsymbol{S}, \quad (5)$$

where $\boldsymbol{u}$ is a vector of conserved quantities, $\boldsymbol{\Pi}$ is the flux tensor, and $\boldsymbol{S}$ is the source term. The system of equations is integrated using finite volume methods. The temporal evolution of equation (5) is carried by explicit methods and the time step is limited by the Courant–Friedrichs–Lewy (CFL; Courant, Friedrichs & Lewy 1928) condition. The code implements time-dependent optically thin cooling ($\dot{e}_{\rm rad}$ in equation 3) and the source terms ($\dot{\rho}_{\rm SN}$ in equation 1 and $\dot{e}_{\rm SN}$ in equation 3) via operator splitting. Our results are unaffected by boundary conditions because we ensure that our box-size is large enough such that the outer shock is sufficiently inside the computational domain. We use the HLLC Riemann solver (Toro, Spruce & Speares 1994). The solution is advanced in time using a second-order Runge–Kutta (RK2) scheme and a total variation diminishing (TVD) linear interpolation is used. The CFL number is set to 0.3 for numerical stability. The computational domain is initialized with an ISM of uniform density (n_{g0}), with a mean molecular weight per particle $\mu = 0.603$ (mean molecular weight per electron $\mu_{\rm e} = 1.156$), and solar metallicity at a temperature of 10^4 K.

We have used the cooling module of PLUTO with the solar metallicity cooling table of Sutherland & Dopita (1993). The cooling function is set to zero below 10^4 K. We do not include self-gravity, disc stratification, magnetic fields, and any form of gas heating (except by thermal energy injection due to SNe) in our simulations.

We have two types of simulation setups:

(i) **Full box:** The full box simulations have a computational domain extending from $-L$ to $+L$ in all three directions. Outflow boundary conditions are used at the boundary of the computational box (i.e. the planes $x = -L, +L$, $y = -L, +L$ and $z = -L, +L$).

(ii) **Octant:** In octant simulations, the simulation box extends from 0 to $+L$ along the three directions. We inject SNe in a spherical 'star cluster' centred at the origin, and the outcomes are spherically symmetric in a statistical sense. Therefore, these simulations are statistically equivalent to the full box simulations, but are computationally less expensive by roughly a factor of 8. These simulations are only carried out for a large number of SNe ($N_{\rm OB} \geq 10^3$) because of a larger spatial stochasticity for small number of SNe; for small $N_{\rm OB}$, an octant may have an effective number of SNe, which is substantially different from $N_{\rm OB}/8$. For precise mass and energy budgeting, we account for the actual mass and energy dumped in by SNe in all cases. Reflective boundary conditions are used at the faces intersecting within the 'star cluster' (i.e. the planes $x = 0$, $y = 0$, and $z = 0$).

2.2 Supernova energy injection

In our setup, SNe explode within a 'star cluster', a spherical region of radius $r_{\rm cl}$ centred at the origin of the simulation box. Most young star clusters are $\lesssim$10 pc in size (e.g. see Larsen 1999) but we allow $r_{\rm cl}$ to be larger. A larger $r_{\rm cl}$ crudely mimics a collection of star clusters that powers global galactic outflows such as in M82 (O'Connell et al. 1995). The locations of SNe are chosen randomly, distributed uniformly within a sphere of radius $r_{\rm cl}$, using the uniform random number generator `ran2` (Press, Flannery & Teukolsky 1986). SNe are injected uniformly in time, with the time separation between successive SNe given by

$$\delta t_{\rm SN} = \frac{\tau_{\rm OB}}{N_{\rm OB}}, \quad (6)$$

where $\tau_{\rm OB}$ (chosen to be 30 Myr) is the lifetime of the OB association and $N_{\rm OB}$ is the total number of SNe (which equals the total number of O and B stars). Ferrand & Marcowith (2010) have shown that statistically the SN rate is uniform. McCray & Kafatos (1987) also show that a constant mechanical luminosity is a good approximation to SN energy injection. Also, it helps to understand the numerical results with simple analytic calculations.

Each SN deposits a mass of $M_{\rm SN} = 5\ {\rm M}_\odot$ and internal energy of $E_{\rm SN} = 10^{51}$ erg over a sphere of size $r_{\rm SN} = 5$ pc; the SN energy injection radius is chosen to prevent artificial cooling losses (see equation 7 in SRNS14, corresponding to their thermal explosion model). SRNS14 found that the late time [after a SN enters the Sedov–Taylor (ST) stage] results are independent of whether SN energy is deposited as kinetic or thermal energy (see their figs 2 and 3), so we simply deposit thermal energy.

Mass and energy injection from each SN is spread in space and time using a Gaussian kernel, such that the mass and internal energy source terms ($\dot{\rho}_{\rm SN}$ in equation 1 and $\dot{e}_{\rm SN}$ in equation 3) are proportional to $\exp(-[t - t_{\rm i}]^2/\delta t_{\rm inj}^2) \times \exp(-[\boldsymbol{x} - \boldsymbol{x}_{\rm i}]^2/r_{\rm SN}^2)$, where ith SN is centred at $t_{\rm i}$ in time and at $\boldsymbol{x}_{\rm i}$ in space. The injection time-scale is chosen to be $\delta t_{\rm inj} = \delta t_{\rm SN}/10$. SN injection with smoothing is found to be numerically more robust and the results are insensitive to the details of smoothing. In addition to thermal energy, we deposit a subdominant amount of kinetic energy because the mass that we add in each grid cell (equation 1) is added at the local velocity. We account for this additional energy in our energy budget.

We have carried out simulations with different values of initial ambient density (n_{g0}), cluster size ($r_{\rm cl}$), and number of SNe ($N_{\rm OB}$). The physical size of the simulation box is chosen according to the number of SNe and the ambient density (based on the adiabatic bubble formula of McCray & Kafatos 1987, the outer shock radius $r_{\rm sb} \propto [N_{\rm OB} t^3/n_{g0}]^{1/5}$). All our 3D simulations are listed in Table B1 (convergence runs for the fiducial parameters, $N_{\rm OB} = 100$, $n_{g0} = 1\ {\rm cm}^{-3}$, $r_{\rm cl} = 100$ pc) and Table 1 (all other runs).

3 RESULTS

3.1 The fiducial run

In this section, we describe in detail the morphology and evolution of a superbubble for number of SNe $N_{\rm OB} = 100$, initial gas density

Table 1. Parameters of our 3D simulations.

$N_{\rm OB}$	$n_{\rm g0}$ (cm^{-3})	$r_{\rm cl}$ ($\times 10^2$ pc)	L (pc)	N	δL (pc)	Sim type F/O	$\delta t_{\rm SN}$ (Myr)	$E^{\ddagger}_{\rm inj}$ ($E_{SN,\,51}$)	$\eta^{\dagger}_{\rm mech}$ (per cent)	$\eta^{\dagger}_{\rm O}$
100	0.1	1.0	1038	410	2.54	O	0.24	12	12.66	1.00
100	0.3	1.0	876	700	2.50	F	0.24	137	11.37	0.98
100	0.5	1.0	779	620	2.51	F	0.24	137	8.70	0.69
100	0.8	1.0	714	570	2.51	F	0.24	136	6.74	0.61
100	2.0	1.0	698	570	2.45	F	0.24	135	3.28	0.22
100	1.0	0.0	714	580	2.46	F	0.24	123	4.66	0.37
100	1.0	0.7	649	300	4.33	F	0.24	131	4.49	0.41
100*	1.0	1.0	649	512	2.54	F	0.24	136	5.72	0.47
100	1.0	1.5	649	300	4.33	F	0.24	130	3.93	0.36
100	1.0	0.3	601	512	2.35	F	0.24	138	6.38	0.44
1000	1.0	1.0	1136	450	2.54	O	0.024	134	5.34	0.94
1000	2.0	1.0	1055	420	2.51	O	0.024	134	3.17	0.44
1000	3.0	1.0	974	385	2.54	O	0.024	134	1.96	0.21
1000	4.0	1.0	909	360	2.54	O	0.024	134	1.25	0.14
1000	5.0	1.0	876	350	2.50	O	0.024	133	0.83	0.12
10^4	5.0	1.0	1006	400	2.52	O	0.0024	1408	1.80	0.86
10^4	6.0	1.0	1006	400	2.52	O	0.0024	1406	1.44	0.58
10^4	8.0	1.0	974	385	2.54	O	0.0024	1405	1.07	0.16
10^4	9.0	1.0	974	385	2.54	O	0.0024	1398	0.38	0.08
10^4	10.0	1.0	860	340	2.54	O	0.0024	1404	0.68	0.07
10^4	10.0	0.5	649	512	2.54	F	0.0024	16274	1.45	0.44
10^4	10.0	1.0	649	512	2.54	F	0.0024	16385	1.49	0.48
10^4	10.0	1.5	649	512	2.54	F	0.0024	15151	1.48	0.47
10^4	10.0	2.0	649	512	2.54	F	0.0024	13971	1.38	0.45
10^4	10.0	2.5	649	512	2.54	F	0.0024	13173	1.29	0.43
10^4	10.0	3.0	649	512	2.54	F	0.0024	12409	1.23	0.44
10^5	1.0	1.0	2110	850	2.48	O	2.4×10^{-4}	16036	4.58	0.92
10^5	10.0	1.0	1363	550	2.48	O	2.4×10^{-4}	15955	1.65	0.92
10^5	20.0	1.0	1233	490	2.52	O	2.4×10^{-4}	15899	1.06	0.83
10^5	30.0	1.0	1136	450	2.54	O	2.4×10^{-4}	15843	0.78	0.47
10^5	40.0	1.0	1071	425	2.52	O	2.4×10^{-4}	15786	0.57	0.09
10^5	50.0	1.0	1006	400	2.52	O	2.4×10^{-4}	15732	0.42	0.05

Notes. ‡The actual energy injected in units of 10^{51} erg; this can be slightly different from $N_{\rm OB}E_{\rm SN}$ because of extra kinetic energy injection; octant runs should inject $\approx E_{\rm SN}/8$ as only one octant is simulated.
$^{\dagger}\eta_{\rm mech}$ (equation 19) and $\eta_{\rm O}$ (equation 13) are averaged over $t = 29$–30 Myr.
*The fiducial run.

$n_{g0} = 1{\rm cm}^{-3}$, and cluster radius $r_{\rm cl} = 100$ pc, which we choose as our fiducial run. The assumed parameters are typical of supershells (e.g. Heiles 1979; Bagetakos et al. 2011; Suad et al. 2014), but as mentioned earlier, $r_{\rm cl}$ is larger than typical cluster sizes. Our spatial resolution is $\delta L = 2.54$ pc (run R2.5 in Table B1). Simulations with different $N_{\rm OB}$ and n_{g0} evolve in a qualitatively similar fashion, the differences being highlighted in Section 3.4. Numerical resolution quantitatively affects our results, although the qualitative trends remain similar. Strict convergence is not expected because thermal and viscous diffusion is required to resolve the turbulent boundary layers connecting hot and warm phases (e.g. Koyama & Inutsuka 2004). A detailed convergence study is presented in Appendix B.

Fig. 1 shows the gas density and pressure slices in the midplane of the simulation domain at times when SNe are effectively isolated (1.27 Myr) and when they have coalesced (9.55 Myr) to form an overpressured superbubble. Since the evolution of a single SN is well known (see e.g. figs 1 and 2 in Kim & Ostriker 2015), in order to compare with superbubble evolution we just briefly review the different phases of SN evolution. An SN shock starts in the free-expansion phase, moving ballistically till the ejecta sweeps up its own mass in the ISM. The next phase is the well-known adiabatic ST phase, which transitions to a radiative snowplow phase with a thin radiative shell. The radius at which an SN enters the ST phase can be written as

$$r_{\rm ST} \approx 4.3 M_{\rm SN,5}^{1/3} n_{\rm g0,1}^{-1/3} \ {\rm pc}, \tag{7}$$

which in all cases is more than twice the grid resolution. Therefore, in our fiducial run we barely resolve the ST phase of the first few SNe. The corresponding ST time-scale is

$$t_{\rm ST} \approx 6 \times 10^{-4} M_{\rm SN,5}^{5/6} E_{\rm SN,51}^{-1/2} n_{\rm g0,1}^{-1/3} \ {\rm Myr}. \tag{8}$$

For SNe going off inside a rarified bubble (in which most subsequent SNe explode), $r_{\rm ST}$ is larger and $t_{\rm ST}$ is longer. In the ST phase, the bubble loses pressure adiabatically. The bubble stops expanding by $\sim$0.5 Myr after which the interior pressure falls below the ambient value. In this state, the shock slows down to the sound speed in the ambient medium and becomes a sound wave. The SN fizzles out by $\sim$1 Myr. The maximum SN bubble size is $\lesssim 50$ pc.

Various stages of a single SN evolution can be seen in the top panels of Fig. 1, which show four isolated SNe that have exploded by 1.27 Myr. The top-left SN (see the projected locations of SNe

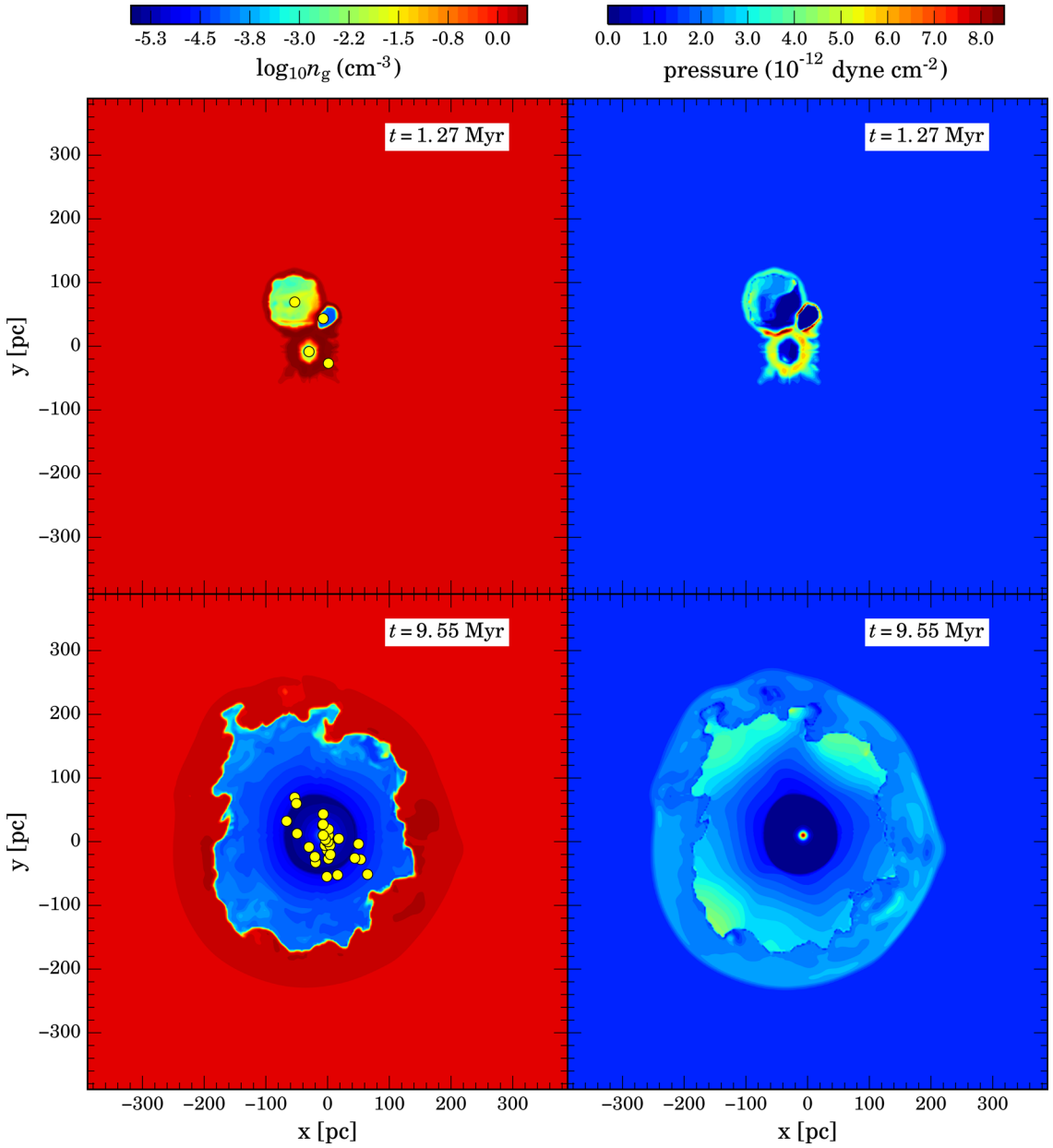

Figure 1. Gas density (left panels; $\log_{10} n_g$[cm^{-3}]) and pressure (right panels) snapshots in the $z = 0$ plane from our fiducial run shown before (top panels) and after (bottom panels) SNe coalesce. The yellow dots mark the *projected* location of SNe in the $z = 0$ plane, with four SNe having exploded by 1.27 Myr and 31 by 9.55 Myr. Top panels show that the SNe at 1.27 Myr are effectively isolated and even at this short time (say, compared to a galaxy's dynamical time) the pressure within their individual bubbles is smaller than the ISM pressure. The bottom panels show the formation of a superbubble due to the overlap of several SNe. The pressure inside most of the bubble volume, except at the centre, is larger than the ISM value. Note that an SN has gone off just before 9.55 Myr, and it creates a high-pressure sphere right at the centre. Also note that while the density scale is logarithmic, the pressure scale is linear.

in the top-left panel) is the oldest, followed by the bottom left one; both have faded away, as can be seen from a relatively high density and low pressure in the bubble region. The other two SNe are younger. The bottom two panels of Fig. 1 show a fully developed superbubble; it is impossible to make out individual SN remnants. Since most stars form in clusters, individual SN remnants are an exception rather than a norm (e.g. see Wang 2014). Most superbubble volume is overpressured (albeit slightly) relative to the ISM. Thus, superbubbles as a manifestation of overlapping SNe are qualitatively different from isolated SNe.

3.1.1 Global mass and energy budget

A key advantage of using a total energy conserving code like PLUTO is that energy is conserved to a very high accuracy and we can faithfully calculate the (typically small) mechanical efficiency of superbubbles. Fig. 2 demonstrates that our mass injection (mimicking SNe) adds $100 M_{\rm SN}$ by 30 Myr, the intended amount. The energy added is higher by ≈30 per cent because, as mentioned earlier, the mass added by the density source term (equation 1) is added at the local velocity, and hence mass addition leads to the addition of kinetic energy.

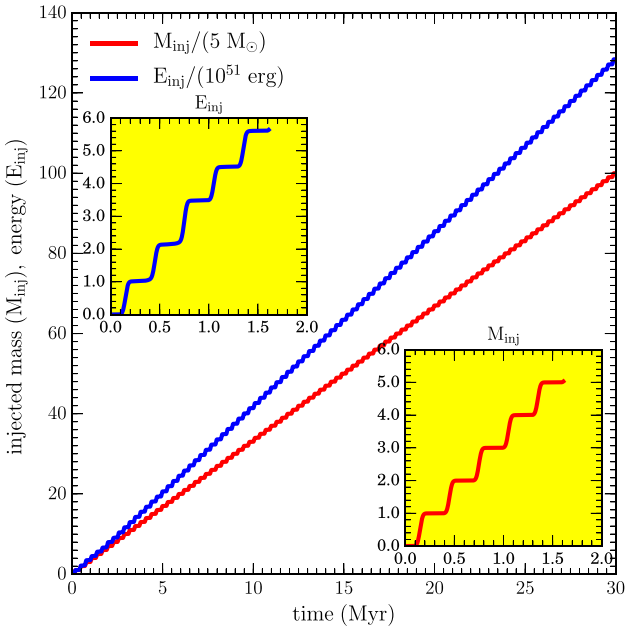

Figure 2. Energy (thermal + kinetic) and mass injected in the simulation box (their value at a given time minus the initial value, normalized appropriately) due to SNe as a function of time for the fiducial run. Injected mass and energy are normalized (5 $M_\odot$ for mass and 10^{51} erg for energy) such that every SN adds 1 unit. Total energy injected is larger than just the thermal energy put in due to SNe by ≈30 per cent because kinetic energy is injected in addition to the dominant thermal energy. The insets at top left and bottom right show a zoom-in of injected energy and mass, respectively. One can clearly see a unit step in the injected mass and energy for each SN that goes off.

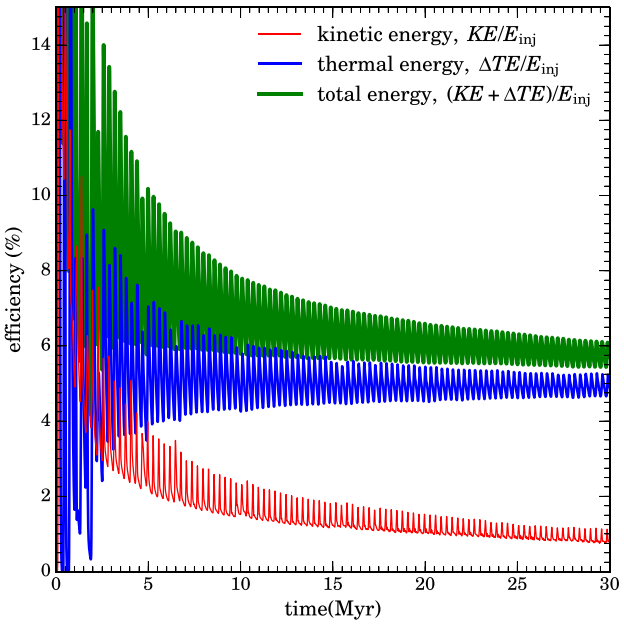

Figure 3. The fraction (percentage) of injected energy retained as kinetic energy and thermal energy of gas inside the simulation box. At the end of the simulation, the gas retains a small fraction, ≈1 per cent and ≈5 per cent of the total injected energy as kinetic energy and thermal energy, respectively. The periodic spikes in energies correspond to individual SNe going off. In the legend, *KE* stands for the kinetic energy and ΔTE for the change in thermal energy within the computational domain.

Fig. 3 shows thermal, kinetic, and total energy efficiency as a function of time for the fiducial run. Energy efficiency is defined as the ratio of excess energy (current minus initial) in the simulation domain and the total energy injected by SNe. The energy efficiency that is higher at early times decreases and asymptotes to a small value. Due to efficient cooling, most (≈95 per cent by 30 Myr) of the deposited energy is lost radiatively. Out of the remaining five, ≈4 per cent is retained as the thermal energy and 1 per cent is retained as the kinetic energy of the gas. In terms of the energy deposited by a single SN, the total (kinetic+thermal) energy retained is $\approx 6\,E_{SN}$.

3.1.2 Density–pressure phase diagram

A bubble (associated with both an individual SN and a superbubble) remains hot and dilute for a long time (several Myr) but is not overpressured with respect to the ISM for a similar duration. The strength of the bubble pressure compared to that of the ambient medium is a good indicator of its strength. As pressure decreases with the expansion of the bubble, it will no longer be able to sustain a strong forward shock and will eventually degenerate into a sound wave.

Fig. 4 shows the volume distribution of pressure at all times for the fiducial run. At $t = 0$, all the gas is at the ambient ISM pressure (indicated by the vertical red line at 1.38×10^{-12} dyne cm^{-2}). Because of a very short-lived high-pressure (ST) phase and a small volume occupied by the very overpressured gas, the volume fraction of gas with pressure $\gtrsim 5 \times 10^{-12}$ is small at all times. Before few Myr, there is no coherent (in time) structure in the

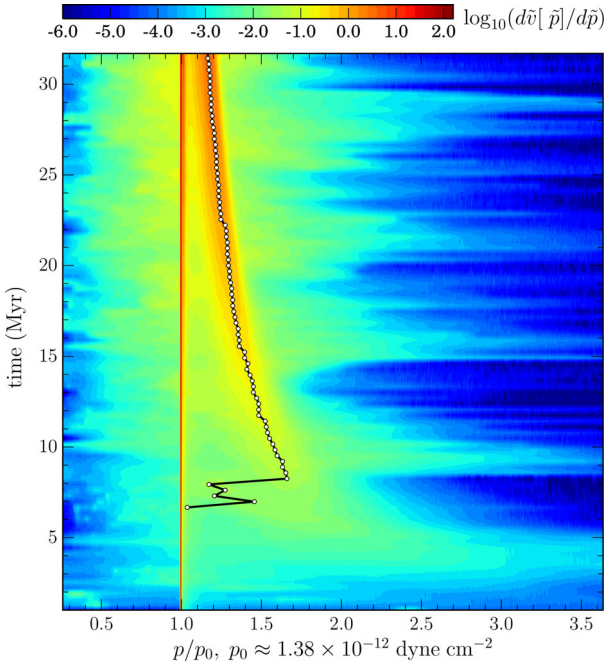

Figure 4. Volume distribution of pressure (along horizontal axis; normalized to the initial value p_0) at different times (along vertical axis) for the fiducial run. Colour represents the volume fraction ($\log_{10}(d\tilde{v}[\tilde{p}]/d\tilde{p})$; $\tilde{v} = v/V$, where $V = 8L^3$ is the volume of the simulation box; $\tilde{p} = p/p_0$; bin-size in pressure $\Delta\tilde{p} = 0.007$) of different pressures at all times. The vertical red line at unity corresponds to the large volume occupied by the ambient unperturbed ISM. The circles connected by a solid line mark the location of the local pressure maximum on the higher side. Before 5 Myr, a coherent overlap of isolated SNe has not happened and a distinct structure in the pressure distribution does not appear.

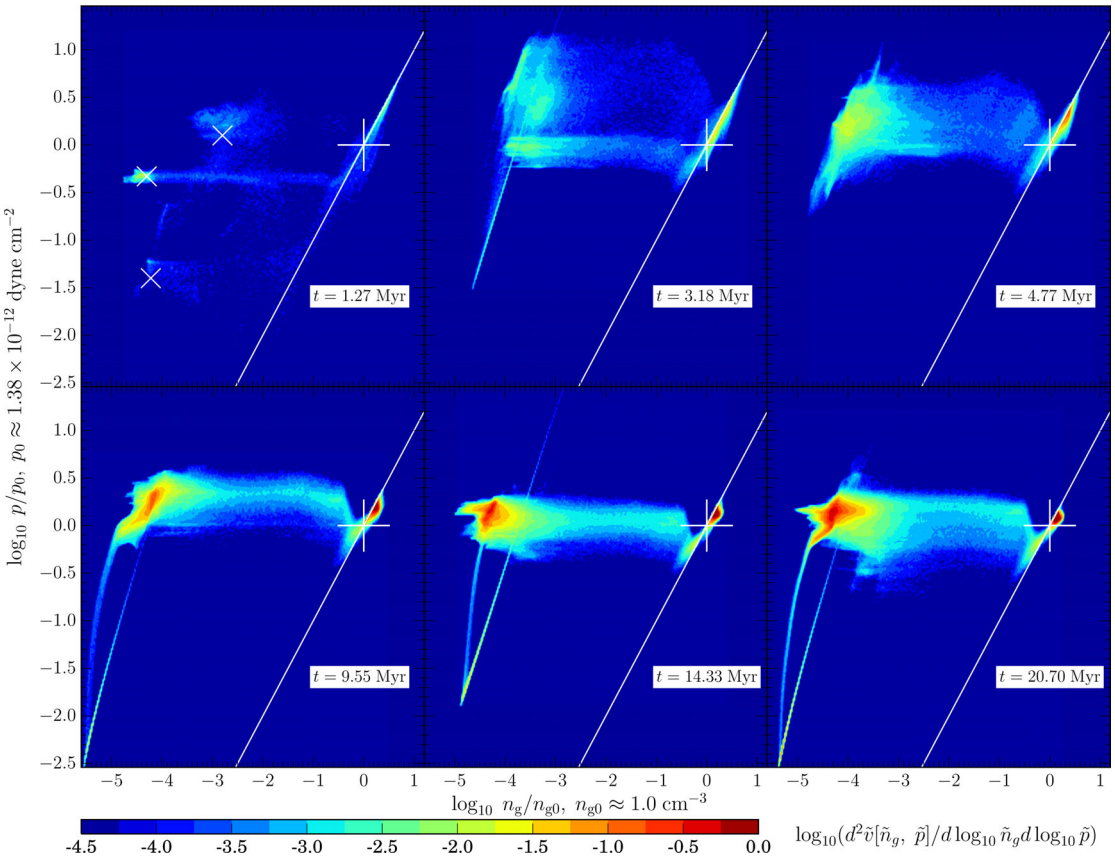

Figure 5. Volume distribution of pressure and gas number density ($d^2\tilde{v}/d\log_{10}\tilde{n}_g d\log_{10}\tilde{p}$; $\tilde{v} = v/V$, $\tilde{n}_g = n_g/n_{g0}$, $\tilde{p} = p/p_0$; the bin-size $\Delta\log_{10}\tilde{n}_g = 0.03$, $\Delta\log_{10}\tilde{p} = 0.01$) for the fiducial run at different times. At late times, there are two peaks in the distribution function corresponding to the WNM (ambient ISM at 10^4 K) and the hot bubble (at $\sim 10^6 - 10^8$ K). At 1.27 Myr, we can see the signatures of non-overlapping SNe fizzling out. Later, after about 5 Myr, we see the formation of a low density and (slightly) over pressured superbubble. At sometimes, we see streaks with $p \propto n_g^{5/3}$, representing adiabatic cooling of recent SNe ejecta expanding in the low-density cavity. The white line shows a temperature of 10^4 K, '+' represents the ambient pressure and density, and 'x's at 1.27 Myr represent bubbles corresponding to individual SNe (the bottom-right SN in the top-left panel of Fig. 1 is very young and not clearly seen).

pressure distribution. After overlap of SNe and the formation of a superbubble, there is a coherent high-pressure peak (shown by the solid line marked by small circles) in the volume distribution that decreases with time. Bubble pressure decreases because of radiative and adiabatic losses. As the input energy is spread over a larger and larger volume the bubble pressure decreases and eventually (much later than for an isolated SN) becomes comparable to the ambient pressure. At this stage, the shell propagates as a sound wave. In short, the first few SNe behave as if they are isolated, and as their remnants grow in size they start overlapping and create a superbubble. In Fig. 4, till 4–5 Myr, the ambient ISM is the most dominant phase. The overlapping of SNe leads to the formation of a second dominant branch in the pressure plot, which is at a higher value than the ambient pressure.

Fig. 5 shows the evolution of gas in the pressure–density plane. The white plus (+) at n_g/n_{g0}, $\tilde{p}_g/p_0 = 1$ marks the location of the ambient ISM. At early times, SNe are isolated as evident from the multiple bright areas (marked with white 'x') in the $p - n_g$ distribution at $t = 1.27$ Myr. Significant volume is occupied by gas at the ambient temperature (10^4 K), which represents dense/isothermal radiative shells of isolated SNe at early times and weak outer shock at later times. As the entire cluster volume is filled with hot gas, it forms an extended hot bubble, and the $p - n_g$ plane shows a bimodal volume distribution in which the shell/ISM gas is on right and the hot ($\sim 10^8$ K) and rarified gas in the bubble is on left. As the superbubble ages, the hot ($\sim 10^8$ K) and warm ($\sim 10^4$ K) phases reach rough pressure equilibrium (most of the superbubble volume is still slightly overpressured; see Fig. 4). However, the bubble gas density, even at late times, is ~4 orders of magnitude smaller relative to the ambient ISM value. In some snapshots (bottom three panels), we see a straight line with slope equal to $\gamma = 5/3$ stretching from low density/pressure to the peak in the hot gas distribution. These streaks represent adiabatic hot winds launched by continuous (for a short time $\delta t_{\rm inj}$) SN energy injection (see Section 2.2) inside the dilute hot bubble (see the very low-density/pressure sphere at the centre in the bottom panels of Fig. 1). The curved streak at low pressure/density is due to smaller energy injection at the beginning (and end) of SN energy injection (recall that energy injection follows Gaussian smoothing in time; see Section 2.2). These streaks are an artefact of our smooth SN energy injection.

3.1.3 Average profiles and overpressure fraction

The radius evolution of a single SN remnant inside a uniform medium is well known. The radius expands differently with time in each of the free-expansion, ST, pressure-driven snowplow, and momentum-conserving phases (e.g. Cox 1972). The radius evolution of a superbubble is qualitatively different from the radius evolution of a single SN because of the continuous injection of

mechanical energy till the lifetime of the OB association (e.g. SRNS14). A large bubble pressure is maintained until the energy (only a small fraction of it is retained due to radiative losses) is spread over a large volume.

The bubble retains only a fraction of injected mechanical energy because of radiative losses. For simplicity, the effects of radiative losses can be incorporated in the adiabatic relations using a mechanical efficiency factor, $\eta_{\rm mech}$. The superbubble radius ($r_{\rm sb}$) and velocity ($v_{\rm sb} = dr_{\rm sb}/dt$) evolve with time as (equation 5 of Weaver et al. 1977)

$$r_{\rm sb} \approx 58 \text{ pc } \eta_{\rm mech,-1}^{1/5} \left(\frac{E_{\rm SN,51} N_{\rm OB,2}}{\tau_{\rm OB,30} n_{g0}} \right)^{1/5} t_{\rm Myr}^{3/5}, \quad (9)$$

$$v_{\rm sb} \approx 34 \text{ km s}^{-1} \eta_{\rm mech,-1}^{1/5} \left(\frac{E_{\rm SN,51} N_{\rm OB,2}}{\tau_{\rm OB,30} n_{g0}} \right)^{1/5} t_{\rm Myr}^{-2/5}, \quad (10)$$

where $E_{\rm SN,\,51}$ is the SN energy scaled to 10^{51} erg, $N_{\rm OB,\,2}$ is the number of OB stars in units of 100, $\tau_{\rm OB,\,30}$ is the age of OB association in units of 30 Myr, n_{g0} is the ambient gas density in cm^{-3}, and $t_{\rm Myr}$ is time in Myr. The mechanical energy retention efficiency $\eta_{\rm mech,\,-1}$ is scaled to 0.1. The supershell velocity can be expressed in terms of its radius as

$$v_{\rm sb} \approx 34 \text{ km s}^{-1} \left(\frac{\eta_{\rm mech,-1} E_{\rm SN,51} N_{\rm OB,2}}{\tau_{\rm OB,30} n_{g0} r_{\rm sb,58pc}^2} \right)^{1/3}. \quad (11)$$

The superbubble weakens after the outer shock speed becomes comparable to the sound speed, i.e. $v_{\rm sb} \approx c_0$ ($c_0 \equiv [\gamma k_B T_0/\mu m_p]^{1/2}$ is the sound speed in the ambient ISM). Thus, using equation (10), the fizzle-out time is

$$t_{\rm fiz} \approx 21.3 \text{ Myr } \eta_{\rm mech,-1}^{1/2} \left(\frac{E_{\rm SN,51} N_{\rm OB,2}}{\tau_{\rm OB,30} n_{g0}} \right)^{1/2} c_{0,1}^{-5/2}, \quad (12)$$

where $c_{0,\,1}$ is the sound speed in the ambient medium in units of 10 km s^{-1}.

Fig. 6 shows density, pressure, and x-velocity profiles along the x-axis for the fiducial run at the same times as the panels in Fig. 5. The evolution of various profiles is as expected. The shell becomes weaker and slower with time and eventually propagates at roughly the sound speed of the ambient medium (c_0). Time evolution of the angle-averaged (unlike Fig. 6, which shows a cut along x-axis) inner and outer shell radii (see Appendix A) is shown in Fig. 7.

The radius and velocity evolution of bubbles are critically dependent on the presence of radiative losses (encapsulated by $\eta_{\rm mech}$; Weaver et al. 1977). In order to assess the strength of a superbubble, it is useful to define an overpressure volume fraction ($\eta_{\rm O}$) as

$$\eta_{\rm O} = \frac{V_>}{V_> + V_<}, \quad (13)$$

where $V_>$ is the volume occupied by gas at pressure $p > 1.5p_0$ and $V_<$ is the volume occupied by gas at $p < p_0/1.5$ (p_0 is the ambient ISM pressure; the choice of 1.5 is somewhat arbitrary). Thus $\eta_{\rm O}$ gives the fraction of volume occupied by high-pressure, hot, and dilute bubble gas. Since we exclude gas close to the ambient ISM pressure in its definition, $\eta_{\rm O}$ is independent of the computational domain and characterizes the bubble pressure. In Fig. 7, we also show the evolution of the hot volume fraction ($\eta_{\rm O}$) as a function of time for the fiducial run. The hot volume fraction drops initially when SNe have not overlapped, but reaches unity after ≈3 Myr, and starts decreasing rapidly after radiative losses become significant and the bubble pressure becomes comparable to the ISM pressure (or equivalently, the shock velocity becomes comparable to the

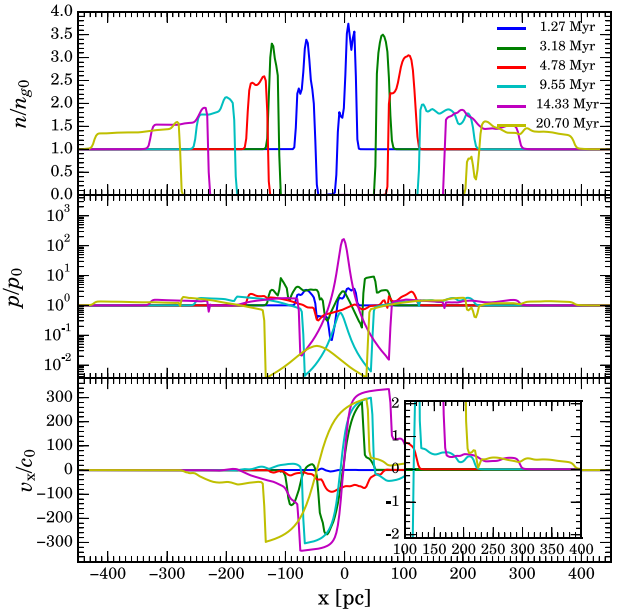

Figure 6. Gas density, pressure and x-velocity profiles along the x-axis ($y = z = 0$) for the fiducial run at various times. The swept-up shell density decreases with time as the superbubble weakens and eventually the shell propagates at the sound speed in the ambient medium ($c_0 \approx 15$ km s^{-1}). As seen in Fig. 1, the bubble density is ∼4 orders of magnitude smaller than the ambient value. The main bubble pressure decreases with time, except during SN injection, during which a high-pressure core and an adiabatic wind with large velocity and small pressure (similar to CC85) forms (the streaks seen in some panels of Fig. 5 are also a signature of this). The inset in the lowest panel shows that the dense shell propagates at about half the sound speed in the ambient ISM, but the velocities in the low-density bubble are much higher.

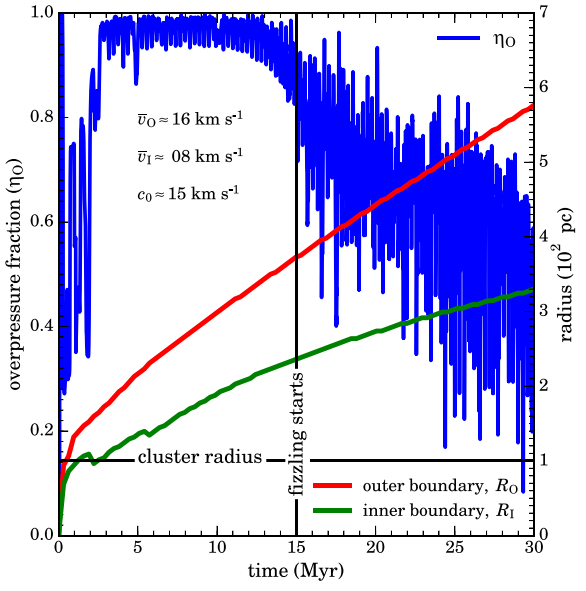

Figure 7. The inner (green line) and outer (red line) radius of the superbubble shell as a function of time for the fiducial run. The blue line shows the overpressure fraction ($\eta_{\rm O}$) as a function of time. The superbubble starts to fizzle out when the overpressure fraction starts falling from ≈1, which happens around 15 Myr. The average outer shell velocity is comparable to the ISM sound speed; the inner shell speed is smaller. The bottom panel of Fig. 6 shows that at late times the shell material moves at ≈$c_0/2$, similar to the inner shell speed. The outer shell velocity is higher, ≈c_0, consistent with the shell density decreasing in time.

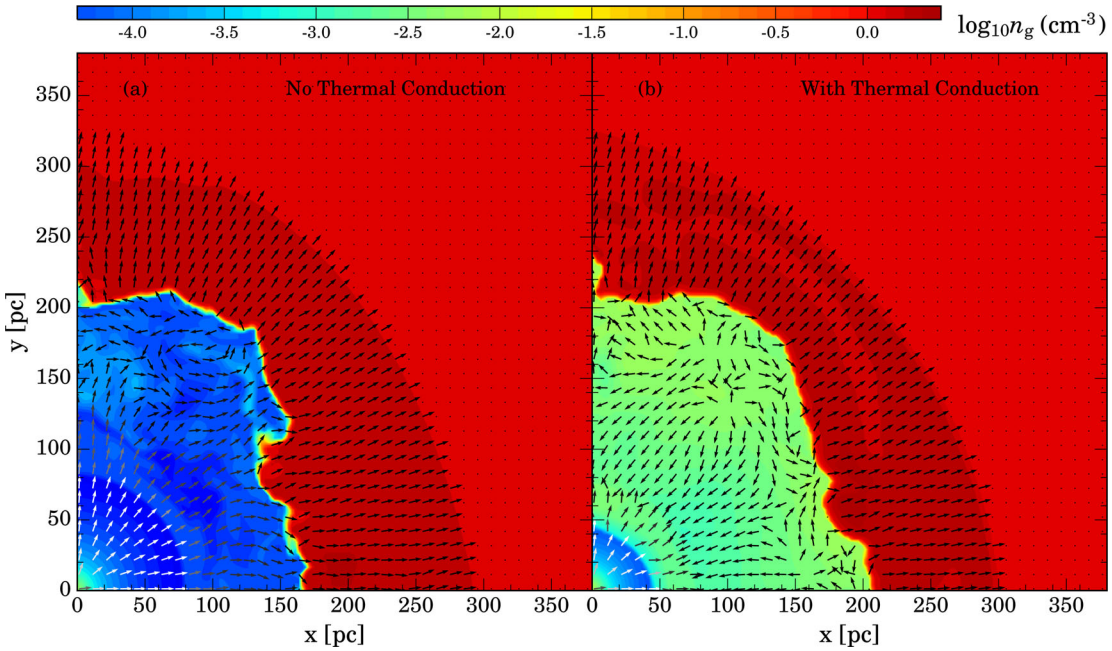

Figure 8. A density contour plot and a quiver plot showing the projection of the velocity unit vector ($\hat{v}$) in the x–y plane for the fiducial simulation with (right panel) and without (left panel) conduction. Note that in the simulation with conduction, there is a region $\approx$ 100–150 pc in which the flow is directed inwards, whereas such a flow is absent in the run without conduction; this flow occurs as conduction leads to evaporation of material from the shell into the bubble. The parameters of these runs are: number of SNe $N_{\rm OB} = 100$, initial gas density $n_{g0} = 1\,{\rm cm}^{-3}$, and cluster radius $r_{\rm cl} = 100$ pc. The snapshots are at $\approx$14.33 Myr.

ISM sound speed). The nature of the hot volume fraction evolution is discussed in more detail in Sections 3.4.2 and 4.1.

3.2 Effects of thermal conduction

We have done the fiducial run with the isotropic thermal conduction module in PLUTO code, which implements *Spitzer* and saturated thermal conduction based on super time stepping (STS; Alexiades, Amiez & Gremaud 1996; $\nu_{\rm STS} = 0.01$). Matter evaporates from the cold shell to the interior of the hot bubble (made of shocked SNe) due to thermal conduction, as shown analytically by Castor et al. (1975) (see also the right panel of fig. 9 in SRNS14). Fig. 8 shows the density snapshots and projected velocity unit vectors for the fiducial run with (right panel) and without (left panel) conduction. The density in the hot bubble is much higher with conduction due to the evaporative flow from the dense shell to the hot bubble, as indicated by the velocity unit vectors in the right panel. Such a flow is absent in the run without conduction. The maximum temperature reached by the gas with conduction is much smaller than without it (cf. Fig. 19). Overall, we find that the thermal conduction does not affect the dynamics of the shell (e.g. its radius and velocity) but affects the temperature distribution of gas within the shell, which can influence its emission/absorption signatures. Since superbubble dynamics is unaffected by thermal conduction, we do not include it in the rest of our simulations.

3.3 Comparison with 1D simulations

Most of SN and superbubble studies are carried out in spherical 1D geometry because these systems are spherical (although only crudely) and very high resolution runs can be done. We want to compare our more realistic 3D simulations (albeit with much lower resolution compared to the modern 1D simulations) with 1D runs to highlight the similarities and differences between the two.

For a realistic comparison of 1D spherical and 3D Cartesian runs, we run a 3D simulation in which we explode all SNe at the origin (i.e. $r_{\rm cl} = 0$). Both the 1D and 3D runs have the same resolution as the fiducial run ($\delta L = \delta r = 2.54$ pc; the only difference between this 3D simulation and the fiducial run is that here $r_{\rm cl} = 0$). As discussed in Section 3.1.1, the amount of total mechanical energy injected in the box is slightly larger than $N_{\rm OB} \times E_{\rm SN}$ because of extra kinetic energy that we put in due to mass addition at the local velocity. For an exact comparison of our 1D and 3D runs, we match the total energy injected in our 1D and 3D runs (by slightly scaling $E_{\rm SN}$ for the 1D run). Three panels of Fig. 9 (except the bottom-right one) compare the time evolution of 1D and 3D simulations. The top two panels show that the total radiative losses are slightly higher (by $\approx$3 per cent) for the 1D spherical run (correspondingly, mechanical energy in the box is slightly smaller), and they are similar for the 3D Cartesian simulations with $r_{\rm cl} = 0$ and $r_{\rm cl} = 100$ pc. The overpressure fraction ($\eta_{\rm O}$) evolution is also very similar for the spherical 1D and the 3D simulation with $r_{\rm cl} = 0$. The rapid fluctuations in $\eta_{\rm O}$ at late times show that the bubble pressure is close to the ISM value and jumps above $1.5p_0$ after every new SN explodes inside it. The outer (inner) shell radius for the 3D simulation (with $r_{\rm cl} = 0$) is only slightly larger (smaller) than the 1D run. To conclude, 1D spherical simulations capture the correct evolution of global (or volume-averaged) quantities such as mechanical efficiency.

The bottom right panel of Fig. 9 shows the radial distribution of emissivity for the three runs. For 3D runs, average pressure and density are obtained by averaging over radial shells of size δL and emissivity ($n_{\rm e} n_{\rm i} \Lambda[T]$) is calculated. The almost discontinuous rise in emissivity corresponds to the contact discontinuity between the shocked SN ejecta and the shocked ISM. While the 1D emissivity profile is very sharp, the transition for 3D runs (particularly with $r_{\rm cl} = 100$ pc) is smoother. This smoothing is due to deviation from sphericity, in particular the crinkling of the contact surface seen in

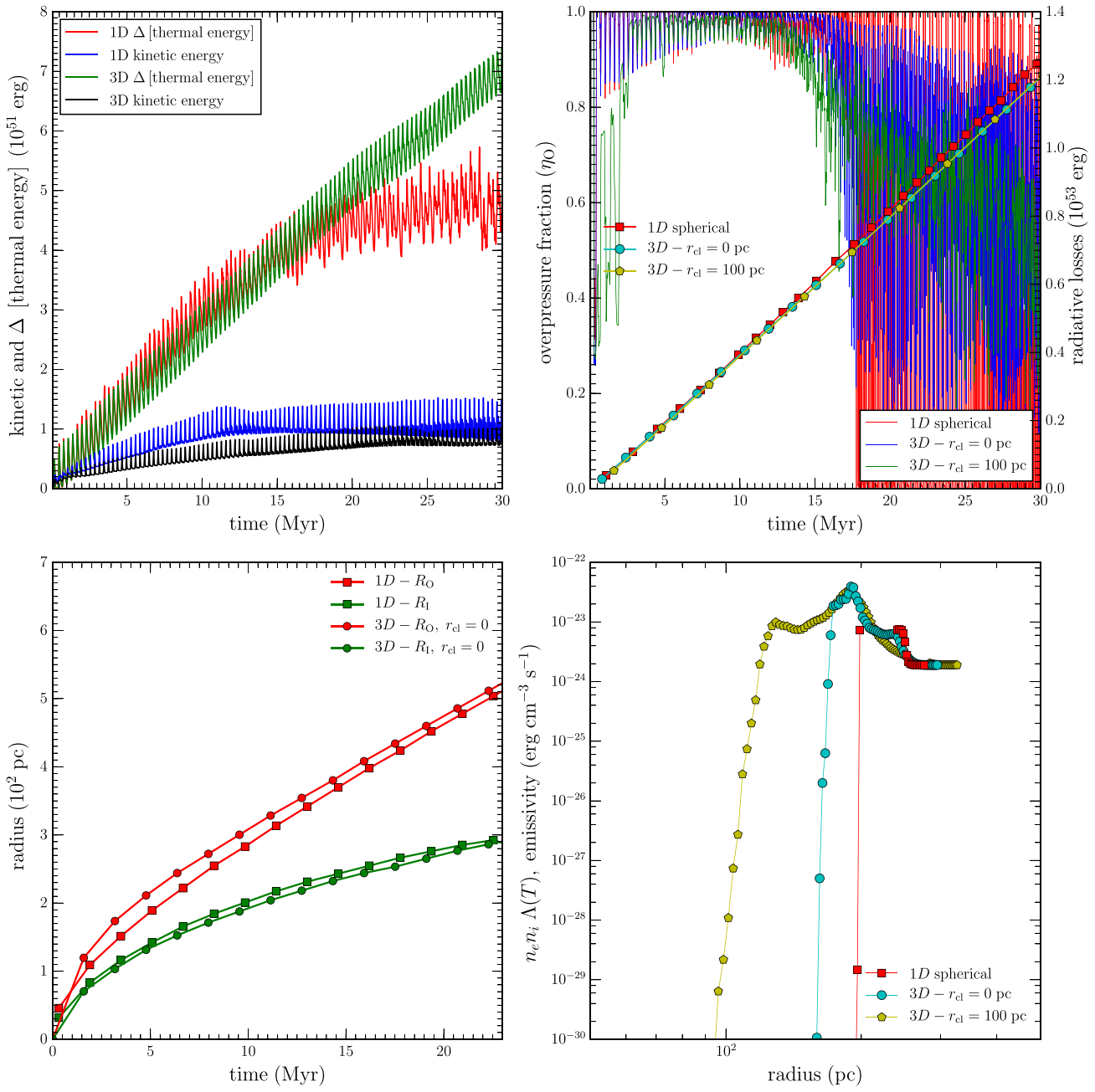

Figure 9. A comparison of 3D (with $r_{cl} = 0$ pc; $r_{cl} = 100$ pc run is also shown for the right panels) and 1D spherical simulations. The top-left panel shows the kinetic and thermal energy added to the box by SNe. The top-right panel shows the overpressure fraction (η_O; solid lines) for the spherical 1D run and the 3D Cartesian runs with $r_{cl} = 0, 100$ pc; also shown in lines connected by symbols are cumulative radiative losses. The bottom-left panel shows the time evolution of the inner and outer shell radius for the 1D and 3D ($r_{cl} = 0$) simulations. The bottom right panel shows the angle-averaged emissivity in the shell for the three simulations at 9.55 Myr (corresponding to the bottom panels of Fig. 1). Note that there is a 'gap' in the emissivity for the 1D spherical run in the dense shell where temperature is $\leq 10^4$ K and we force $\Lambda[T] = 0$.

the bottom panels of Fig. 1. This also makes the shell in Cartesian simulations slightly thicker compared to the spherical 1D run. Radiative losses for 3D runs are spread almost throughout the shell but are confined to the outer radiative relaxation layer in the spherical run (see fig. 5 in SRNS14).

Both the 1D and 3D simulations show that the bubbles are smaller than the analytic estimates because of radiative cooling. Even in a uniform medium, the shell can be unstable to various 3D instabilities such as 'Vishniac instability' (Vishniac 1983), which affects the morphology of supershells (cf. Fig. 13; see also Krause et al. 2013).

3.4 Effects of cluster and ISM properties

After discussing the fiducial run in detail, in this section, we study the influence of cluster and ISM parameters (cluster radius r_{cl}, number of OB stars N_{OB}, and ISM density n_{g0}).

3.4.1 Effects of ISM density

The gas density in which SNe explode is a crucial parameter that determines their subsequent evolution, both in adiabatic

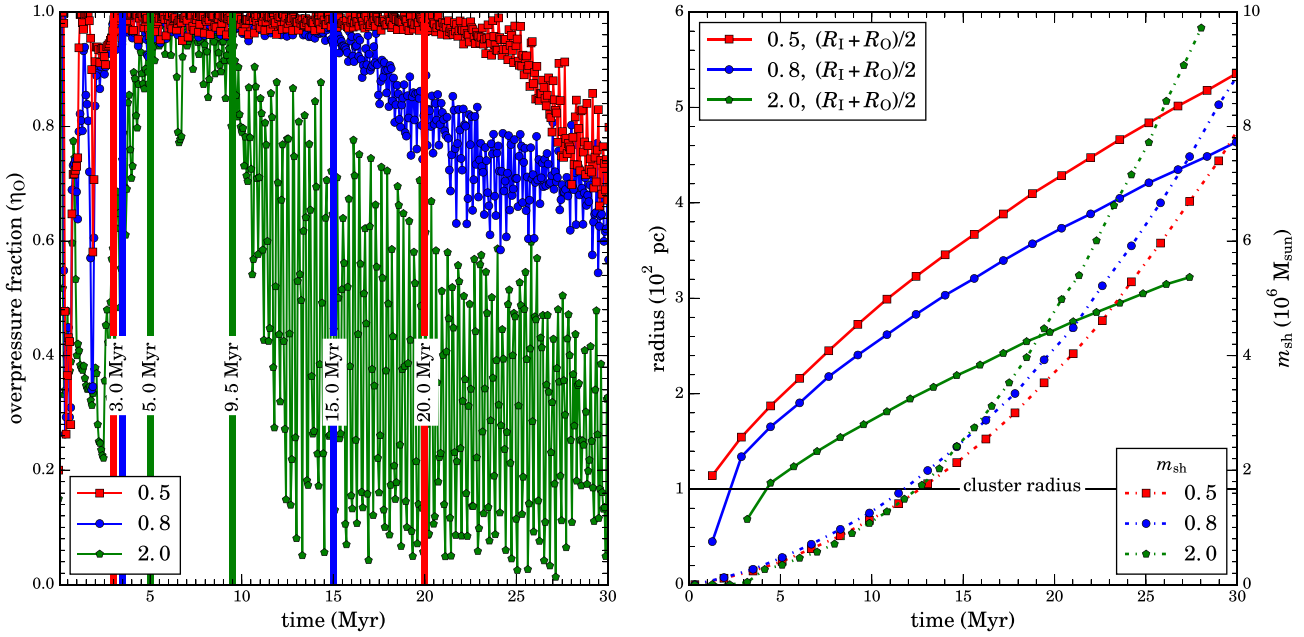

Figure 10. The influence of ambient ISM density ($n_{g0} = 0.5, 0.8, 2$ cm^{-3}) on the overpressure fraction (η_O; left panel), and the inner and outer shell radii (R_I, R_O) and the swept-up mass in the shell (m_{sh}; right panel) for $N_{OB} = 100$ and $r_{cl} = 100$ pc. The vertical lines in the left panel mark the times when SNe overlap and produce an overpressured bubble and times when they fizzle out due to radiative and adiabatic losses. The bubble expanding in the lower density medium expands faster and sweeps up smaller mass.

($r_{sb} \propto \rho^{-1/5}$) and radiative (radiative losses are higher for a larger density) regimes. The left panel of Fig. 10 shows that the overpressure fraction at early times (<5 Myr) both falls and rises slowly for a higher density ISM. The overlap of SNe at higher densities takes longer because the individual bubble radius is smaller for a higher density and one needs to wait longer to fill the whole cluster with hot gas. At late times, the overpressure fraction drops earlier for higher densities because of larger radiative losses (although the bubble pressure scales as $n_{g0}^{3/5}$ according to Weaver et al. 1977 adiabatic scaling).

The right panel of Fig. 10 shows that the bubble expands more rapidly in the lower density medium. It also shows that although the shell in a higher density ISM expands slowly, it sweeps up more mass. An adiabatically expanding strong bubble in a uniform medium is expected to sweep up gas at a rate $\propto n_{g0}^{2/5} t^{9/5}$. Therefore, the ratio of mass swept by the shells with $n_{g0} = 0.5, 0.8$ cm^{-3} shown in Fig. 10 is expected to be $(0.5/0.8)^{2/5} \approx 0.8$, whereas the actual value is ≈0.9. This is because the bubble expanding in a denser ISM is slower than the adiabatic model due to radiative losses; moreover, shells in a higher density medium suffer larger radiative losses. The shell for the highest density run ($n_{g0} = 2$ cm^{-3}) sweeps up an increasingly larger mass at later times because $R_O \propto c_0 t$ at late times, when the shell moves close to the ISM sound speed.

3.4.2 *Effects of cluster radius*

The key difference of this work from SRNS14 is that we are doing 3D simulations, which are necessary to study a realistic spatial distribution of SNe. In 1D spherical setup, all SNe can only explode at the origin because of spherical symmetry. Fig. 11 shows the

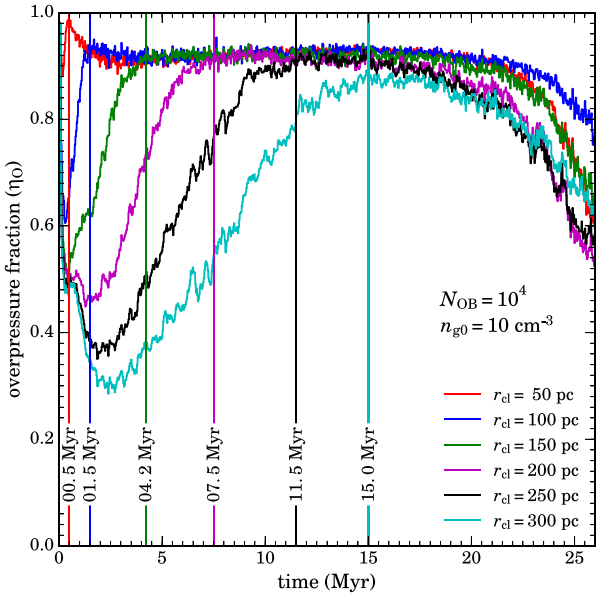

Figure 11. The evolution of overpressure fraction as a function of time for $n_{g0} = 10$ cm^{-3} and $N_{OB} = 10^4$, but with different star-cluster sizes (r_{cl}). The overpressure fraction plummets initially as SNe are effectively isolated and cool catastrophically within 1 Myr. After that, as more SNe go off, they start to overlap and create an overpressured bubble. As expected, the transition to overlap happens later for a larger star cluster. The late time drop in overpressure fraction, occurring due to adiabatic and radiative losses, is similar for different r_{cl}. This suggests that the superbubble evolution is independent of the cluster size, once the coherent overlap of SNe occurs.

evolution of overpressure volume fraction ($\eta_{\rm O}$) as a function of time for simulations with $N_{\rm OB} = 10^4$, $n_{g0} = 10\ {\rm cm}^{-3}$, and different star-cluster radii.[1] The plot has a characteristic shape with an initial fall, a rise and saturation, and an eventual fall. The initial fall occurs as isolated SNe, without overlapping, fizzle out due to radiative losses (the top panels of Fig. 1 show density and pressure in this stage). The rise happens as SNe overlap and form a superbubble. Eventually, the overpressure volume fraction drops as the volume of the superbubble becomes too large and the outer shock weakens due to adiabatic and radiative losses.

We can estimate the time when SNe *start to overlap*. The radius of an isolated SN remnant is given by $r_{\rm SNR} \sim (E_{\rm SN}t^2/\rho)^{1/5}$. Suppose $n_{\rm t}$ SNe have gone off independently by some time t. The volume occupied by the non-overlapping SN remnants is $\sim \sum_{i=1}^{n_t}(4\pi/3)(E_{\rm SN}i^2\delta t_{\rm SN}^2/\rho)^{3/5} \sim (4\pi/3)(E_{\rm SN}\delta t_{\rm SN}^2/\rho)^{3/5}\sum_{i=1}^{n_t} i^{6/5} \sim (4\pi/3)(E_{\rm SN}\delta t_{\rm SN}^2/\rho)^{3/5}(5/11)(tN_{\rm OB}/\tau_{\rm OB})^{11/5}$. Equating this volume with the volume of the star cluster $4\pi r_{\rm cl}^3/3$ gives an estimate for the time when SNe start to overlap ($t_{\rm o,\,ad}$, estimate for SNR overlap assuming adiabatic evolution),

$$t_{\rm o,ad} \sim 0.16\ {\rm Myr}\ \tau_{\rm OB,30}^{5/11} N_{\rm OB,4}^{-5/11} E_{\rm SN,51}^{-3/11} n_{g0,1}^{3/11} r_{\rm cl,2}^{15/11}, \quad (14)$$

where $n_{g0,\,1}$ is gas number density in units of 10 cm^{-3} and $r_{\rm cl,\,2}$ is the radius of the star cluster in units of 100 pc. Note that we have used equation (6) to obtain the above equation.

We can make another estimate for the SN overlap time-scale by assuming that SNe overlap only after they have become radiative. In this case, by a similar argument as that of the last paragraph, the overlap time $t_{\rm o,\,rad}$ is given by $\tau_{\rm OB}/N_{\rm OB}(r_{\rm cl}/r_{\rm b,\,rad})^3$, where $r_{\rm b,rad} \sim 37\ {\rm pc}\ E_{\rm SN,51}^{1/3} n_{g0}^{-1/3}$ (equation 2 in Roy et al. 2013) is the hot/dilute bubble radius when the remnant becomes radiative. Note that the bubble radius does not increase by more than a factor of 2 after this time (e.g. fig. 2 in Kim & Ostriker 2015). Thus, the overlap time, assuming a radiative bubble, is given by

$$t_{\rm o,rad} \sim 0.6\ {\rm Myr}\ \tau_{\rm OB,30} N_{\rm OB,4}^{-1} E_{\rm SN,51}^{-1} n_{g0,1} r_{\rm cl,2}^3. \quad (15)$$

The evolution seen in Fig. 11 lies somewhere in between equations 14 and 15.

The time for the overpressure volume to saturate after overlap of SNe and *transition to a superbubble* evolution is given by (using Weaver et al. 1977 scaling and setting the superbubble shell radius equal to the cluster radius),

$$t_{\rm sb} \sim 1.2\ {\rm Myr}\ r_{\rm cl,2}^{5/3} N_{\rm OB,4}^{-1/3} \eta_{\rm mech,-1}^{-1/3} E_{\rm SN,51}^{-1/3} t_{\rm OB,30}^{1/3} n_{g0,1}^{1/3}, \quad (16)$$

where we have scaled the result with a mechanical efficiency $\eta_{\rm mech}$ of 0.1 (i.e. only ∼10 per cent of the input SN energy goes into blowing the superbubble; ∼90 per cent is lost radiatively). This estimate for the time of superbubble formation roughly matches the results in Fig. 11. Finally, the time when the superbubble pressure ($\sim 0.75\rho v_{\rm sb}^2$) falls to ≈1.5 times the ISM pressure is given by (apart from factors of order unity, this is essentially the same as equation 12)

$$t_{\rm fiz} \sim 10.3\ {\rm Myr}\ T_4^{-5/4} \eta_{\rm mech,-1}^{1/2} E_{\rm SN,51}^{1/2} \tau_{\rm OB}^{-1/2} N_{\rm OB,4}^{1/2} n_{g0,1}^{-1/2}, \quad (17)$$

(T_4 is the ISM temperature in units of 10^4 K) which is only slightly lower than the time corresponding to the late time drop in the overpressure volume fraction in Fig. 11. Note that unless the cluster size ($r_{\rm cl}$) is unrealistically large, overlap of SNe is likely to occur. In this state, the time for a superbubble to fizzle out is independent of the cluster size.

[1] Here we choose parameters ($N_{\rm OB}, n_{g0}$) different from the fiducial run because the different stages of evolution are nicely separated in time for this choice. The temporal behaviour is expected to be qualitatively similar for different choice of parameters.

3.4.3 *Effects of SN rate: formation of a steady wind*

CC85 found a solution for the wind driven by internal energy and mass deposited uniformly within an injection radius ($r < R$). This was applied to the galactic outflow in M82. For a large number of SNe (i.e. a large $N_{\rm OB}$), the mechanical energy injection can be approximated as a constant luminosity wind, $L_w = N_{\rm OB}E_{\rm SN}/\tau_{\rm OB}$. According to CC85, within the injection radius ($r \lesssim R$) the mass density is constant, whereas at large radii (wind region, $r \gtrsim R$) density is expected to be $\propto r^{-2}$. A termination shock is expected at the radius where the wind ram pressure balances the pressure inside the shocked ISM. For small $N_{\rm OB}$, however, the individual SN ejecta does not thermalize within the termination shock radius ($r_{\rm TS}$) as the SN occurs inside a low-density bubble (the bubble density is low in the absence of significant mass loading as most of the ambient gas is swept up in the outer shell) created by the previous SNe. For a large SN rate, the solution should approach the steady state described by CC85. SRNS14 derived analytic constraints on $N_{\rm OB}$ required for the existence of a smooth CC85 wind inside the superbubble (see their equation 11) as

$$\delta t_{\rm SN,CC85} \gtrsim 0.008\ {\rm Myr}\ E_{\rm SN,51}^{-9/26} t_{\rm Myr}^{4/13} n_{g0}^{-3/13} M_{\rm SN,5\odot}^{15/26}, \quad (18)$$

where $M_{\rm SN,\,5\odot}$ is the SN ejecta mass and $t_{\rm Myr}$ is the age of the starburst in Myr. This time between SNe corresponds to a requirement of $N_{\rm OB} \gtrsim 4 \times 10^3$ for a smooth CC85 wind to appear by 1 Myr. Using the standard stellar mass function, this corresponds to a star formation rate (SFR) of $\sim 0.01 {\rm M}_\odot\ {\rm yr}^{-1}$. This is a lower limit because thermalization just before the termination shock does not lead to a high density/emissivity core, the characteristic feature of a CC85 wind. Fig. 12 shows the density profiles for a range of $N_{\rm OB}$ ($N_{\rm OB} = 10^5$ corresponds to a SN rate of $\sim 0.003\ {\rm yr}^{-1}$). As expected from thermalization of a SN within the ejecta of all previous SNe (equation 18), a smooth CC85-type wind with density $\propto r^{-2}$ at 30 Myr only forms for $N_{\rm OB} \gtrsim 10^4$. Since SNe form in OB associations, they are expected to overlap and form superbubbles. For a sufficiently large number of SNe ($\gtrsim 10^5$; e.g. in the super star clusters powering a galactic wind in M82), a strong termination shock (with Mach number $\gg$1) exists till late times, which may accelerate majority of Galactic and extragalactic high-energy cosmic rays (e.g. Parizot et al. 2004). In contrast, strong shocks (especially the reverse shock; McKee 1974) in isolated SNe exist only at early times ($\lesssim 10^3$ yr), after which the reverse shock crushes the central neutron star and the outer shock weakens with time (in fact catastrophically after it becomes radiative).

Fig. 13 shows the 2D density snapshots of the 3D runs shown in Fig. 12, albeit at an earlier time. As expected, the shell is much thinner for a larger number of SNe. Also, a dense injection region and a clear termination shock are visible for the runs with $N_{\rm OB} \gtrsim 10^4$. Crinkling of the contact discontinuity and the thin shell is the key difference of 3D runs as compared to the spherical 1D simulations.

The SNe-driven wind is able to maintain a strong non-radiative termination shock that is able to power the outward motion of the outer shock. The CC85 model has two parameters: the efficiency with which star formation is converted into thermal energy ($\alpha \equiv \dot{E}/{\rm SFR}$), and the mass loading factor ($\beta \equiv \dot{M}/{\rm SFR}$), which

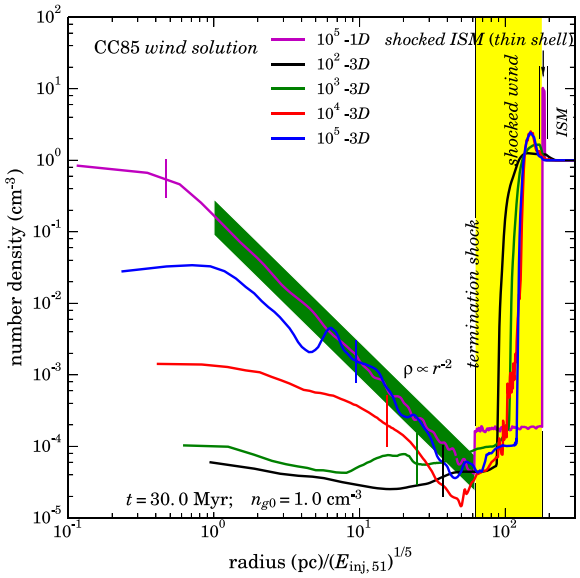

Figure 12. Spherically averaged gas density profiles for 3D runs at 30 Myr ($r_{\rm cl} = 100$ pc, except for the 1D spherical run; $n_{g0} = 1$ cm^{-3}) with various $N_{\rm OB}$. Radius has been scaled with the expected scaling ($E_{\rm inj,51}^{1/5} \approx N_{\rm OB}^{1/5}$ is the total mechanical energy injected in units of 10^{51} erg; see Table 1). The thin vertical lines mark the cluster radius ($r_{\rm cl}$) in the scaled unit. The density profile attains a smooth, steady CC85 profile (its signature is the $\rho \propto r^{-2}$ profile beyond a core region) within the bubble for a large $N_{\rm OB} \gtrsim 10^4$, consistent with the analytic considerations in section 4.3 of SRNS14 (see also fig. 3 in their paper). The radiative shell in 1D run (with the same resolution as the 3D run) is much thinner as compared to 3D because the 3D shell is not perfectly spherical and the contact discontinuity is crinkled (see Fig. 13). The outer shock is weaker for a smaller $N_{\rm OB}$ but its location scales with the analytic scaling ($\propto N_{\rm OB}^{1/5}$).

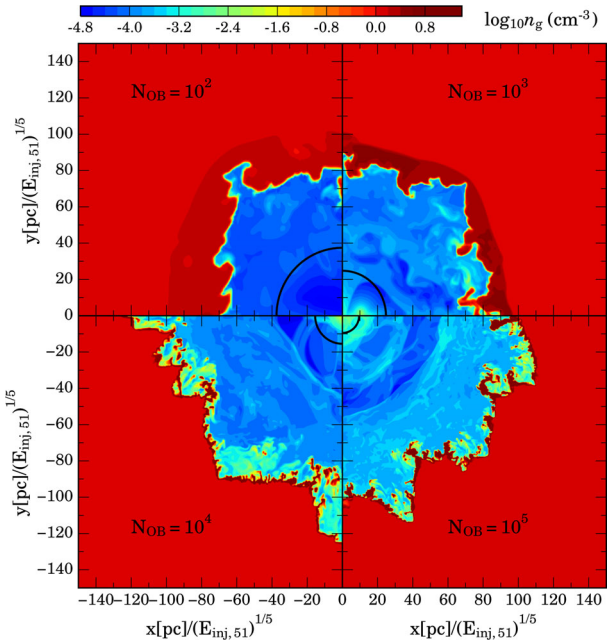

Figure 13. Density slices at $t = 9.55$ Myr in the $x - y$ ($z = 0$) plane for runs with different $N_{\rm OB}$ but with the same ISM density and cluster radius ($n_{g0} = 1$ cm^{-3} and $r_{\rm cl} = 100$ pc). The shell becomes progressively thinner with increasing $N_{\rm OB}$ because a stronger shock causes higher compression. Like Fig. 12, the axes are scaled with respect to the analytic scaling. The solid black arcs mark the cluster radius. A termination shock and a high-density injection region are visible in the bottom two panels.

determine the properties of galactic outflows (e.g. Sarkar et al. 2016). From our setup, we can determine the mass loading for large $N_{\rm OB}$ simulations by calculating the mass-loss rate from the cluster measured at radii where the mass outflow rate $\dot{M}(r) \equiv 4\pi r^2 \rho v$ is roughly constant. The mass loading factor for our $N_{\rm OB} = 10^5$ run is $\approx$1 as most of the SN injected mass flows out in a roughly steady wind. For much larger $N_{\rm OB}$ (or equivalently, SFR) valid for starbursts, the mass loading factor can be reduced because of radiative cooling and mass drop-out from the dense ejecta of SNe (e.g. Wünsch et al. 2007, 2008, 2011). Girichidis et al. (2016) have investigated launching of galactic outflows based on multi-physics simulations which include variation in SN rate and various strategies for placing SNe (random, or at density peaks or isolated). Pakmor et al. (2016) and Simpson et al. (2016) investigate the effect of cosmic ray diffusion on dynamics of galactic outflows. We will investigate the effect of additional processes in our future work.

4 DISCUSSION

In this section, we discuss the astrophysical implications of our work, focusing on radiative losses, comparison the observed H I supershells, and gas expulsion from star clusters.

4.1 Mechanical efficiency and critical supernova rate for forming a superbubble

While isolated SNe lose *all* their energy by $\sim$1 Myr, even overlapping SNe forming superbubbles lose majority of energy injected by SNe. The mechanical efficiency of superbubbles is defined as

$$\eta_{\rm mech} \equiv \frac{(KE + \Delta TE)}{E_{\rm inj}}, \tag{19}$$

where KE is the total kinetic energy of the box, ΔTE is the increase in the box thermal energy, and $E_{\rm inj}$ is the energy injected by SNe (which is slightly larger than $N_{\rm OB}E_{\rm SN}$ because mass is added at the local velocity). By energy conservation (the computational box is large enough that energy is not transported into or out of it), $\eta_{\rm mech} = 1 - RL/E_{\rm inj}$, where RL are cumulative radiative losses. Fig. 14 shows the mechanical efficiency (equation 19) as a function of the initial gas density (n_{g0}) at various times for runs with different $N_{\rm OB}$. One immediately sees that mechanical efficiency decreases with an increasing ISM density (n_{g0}). Efficiency also decreases with time (by almost a factor of 10 from 5 to 30 Myr), especially for higher densities. The maximum efficiency is $\sim$20 per cent, occurring at early times. Our simulations show that the mechanical efficiency of 3D and 1D simulations is comparable and almost independent of the cluster size ($r_{\rm cl}$, see Section 3.3 and Fig. 9), provided that SNe overlap before fizzling out. A rough scaling of $\eta_{\rm mech} \propto n_{g0}^{-2/3}$, valid at most times, can be deduced from Fig. 14. Also note that the mechanical efficiency increases very slightly for a larger number of SNe.

Fig. 14 shows mechanical efficiencies that are about an order of magnitude smaller than the values quoted in SRNS14. For example, the efficiency (which equals 1 fractional radiative losses; see the right panel of fig. 8 in SRNS14) for $N_{\rm OB} = 10^5$ and $n_{g0} = 1$ cm^{-3} in SRNS14 at 30 Myr is $\approx$40 per cent. The value for the same choice of parameters from Fig. 14 is $\approx$6 per cent, smaller by a factor of $\approx$7. This discrepancy is mainly due to the much higher resolution in the 1D simulations of SRNS14 (see Section 4.4).

Fig. 11 shows that the overpressure volume fraction $\eta_{\rm O}$ for $n_{g0} = 10$ cm^{-3} and $N_{\rm OB} = 10^4$ has a similar value for cluster sizes as large

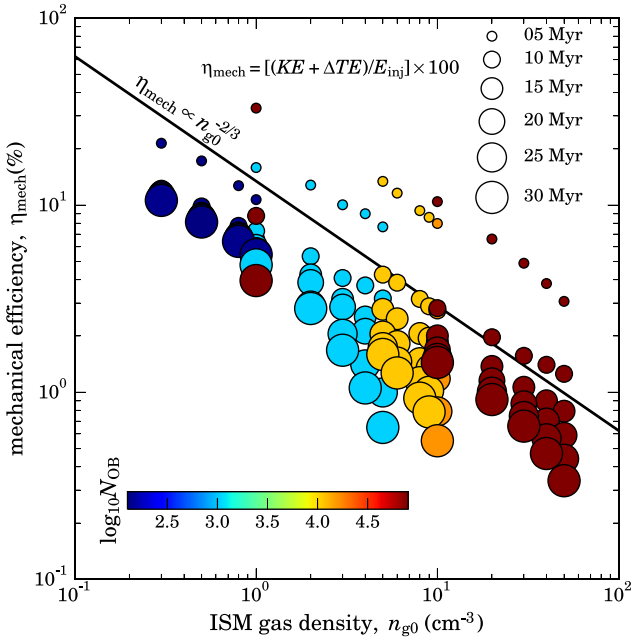

Figure 14. Efficiency of mechanical energy retention in superbubbles as a function of ISM density for different simulations. Clearly, the efficiency decreases with an increasing density because of radiative losses. Colours represent N_{OB} and the sizes of circles stand for different times. Note that for the same density, a higher N_{OB} gives a slightly larger mechanical efficiency. The black solid line shows the $n_{g0}^{-2/3}$ scaling of η_{mech}, which describes well the variation of mechanical efficiency with the ambient density at almost all times. For most runs, especially with high ambient densities ($n_{g0} \gtrsim 2$ cm^{-3}), the mechanical efficiency decreases by almost a factor of 10 from 5 to 30 Myr.

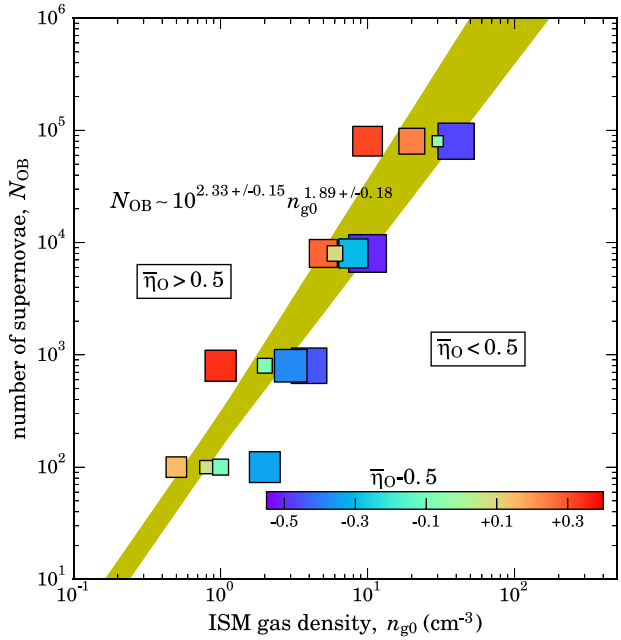

Figure 15. Critical N_{OB} required for a given density of the ISM for the superbubble to remain sufficiently overpressured at late times. The colour bar and the size of squares (a smaller square means that $\bar{\eta}_O$ is closer to 0.5) represent deviation from an average overpressure fraction of 0.5 at late times (25 to 30 Myr). The best-fitting power-law scaling is indicated, and $3-\sigma$ spread about the best fit is indicated by the shaded region.

as $r_{cl} = 300$ pc. This means that the evolution of the superbubble is independent of r_{cl}, as long as overlap of SNe happens before the cluster age, which is very likely not only for individual star clusters but also for clusters of star clusters as in the centre of M82 galaxy (O'Connell et al. 1995). Therefore, the key parameter that determines if the superbubble remains sufficiently overpressured by the end of the star-cluster lifetime, for a given gas density, is the number of SNe N_{OB} (and not the cluster size r_{cl}).

The overpressure volume fraction (defined in equation 13) is an appropriate diagnostic to determine if a superbubble has fizzled out or not. As described earlier, we consider a superbubble fizzled out if the average overpressure fraction falls below 0.5 at late times (25 to 30 Myr). Fig. 15 shows the plot of critical number of SNe required to produce an average overpressure volume fraction of 0.5 at late times (25 to 30 Myr), for a given gas density. We vary the ISM density for a given N_{OB}, such that the late-time overpressure fraction is close to 0.5. The critical N_{OB} roughly scales as n_{g0}^2.

Now we turn to analytic arguments to understand the scaling of critical N_{OB} for a given ISM density (n_{g0}). The superbubble pressure as a function of time, according to the adiabatic model of Weaver et al. (1977), is $\sim \frac{3}{4}\rho v_{sb}^2$, which at the end of cluster lifetime becomes

$$\frac{p_{sb,late}}{k_B} \sim 1.7 \times 10^5 \text{ K cm}^{-3} N_{OB,4}^{2/5} \eta_{mech,-2}^{2/5} \tau_{OB,30}^{-6/5} n_{g0,1}^{3/5}, \quad (20)$$

where mechanical efficiency has been scaled to 0.01. Equating this to 1.5 times the ambient ISM pressure $p_{ISM}/k_B = 10^5 n_{g0,1} T_4$ gives

$$N_{OB,crit} \sim 7.3 \times 10^3 \eta_{mech,-2}^{-1} \tau_{OB,30}^3 n_{g0,1} T_4^{5/2}. \quad (21)$$

This estimate of the critical number of OB stars to maintain an overpressured bubble at late times agrees with Fig. 15 in that the critical N_{OB} for $n_{g0} = 10$ cm^{-3} is about 10^4. From equation (21), we get the scaling of critical N_{OB} as $N_{OB,crit} \propto n_{g0}\eta_{mech}^{-1}$, which when we use the dependence of η_{mech} on n_{g0} from Fig. 14 ($\eta_{mech} \propto n_{g0}^{-2/3}$) gives $N_{OB,crit} \propto n_{g0}^{5/3}$. This scaling is similar to the scaling of critical N_{OB} observed in Fig. 15; namely

$$N_{OB,crit} \approx 200 n_{g0}^{1.89} \tau_{OB,30}^3 T_4^{5/2}. \quad (22)$$

A steeper η_{mech} versus n_{g0}, which is not inconsistent with Fig. 14, will give an even better match. The important point to note is that a decreasing mechanical efficiency with an increasing ISM density is required to explain the critical N_{OB} curve.

The scaling between N_{OB} and gas density (hereafter critical curve) in Fig. 15 can be compared with the empirical relation between SFR and gas density. The Kennicutt–Schmidt (hereafter KS) relation (Schmidt 1959; Kennicutt 1998) between gas surface density and SFR surface density is

$$\frac{\Sigma_{SFR}}{\text{M}_\odot \text{ yr}^{-1} \text{ kpc}^{-2}} \approx 3 \times 10^{-3} \left(\frac{\Sigma_g}{10 \text{ M}_\odot \text{ pc}^{-2}} \right)^{1.4}, \quad (23)$$

which is valid for $\Sigma_g \geq 10$ M$_\odot$ pc^{-2}, below which a much steeper relation holds (Bigiel et al. 2008). Consider a scale height (H) of 100 pc and a disc radius (R_d) of 1 kpc. For each OB star, the total stellar mass is $\sim$100 M$_\odot$ for Kroupa/Chabrier initial mass function (Kroupa 2002; Chabrier 2003). Then for a star formation time-scale of 30 Myr, we have $\Sigma_{SFR} \approx 10^{-6} N_{OB}$ M$_\odot$ yr^{-1} kpc^{-2} $\tau_{OB,30}^{-1} R_{d,kpc}^{-2}$. For a gas density of n_{g0} cm^{-3}, we also have $\Sigma_g \approx 3\, n_{g0} H_{100pc}$ M$_\odot$ pc^{-2} for mean molecular weight $\mu = 1.3$ (assuming

neutral/molecular disc). Therefore, the KS relation can be re-written in terms of the parameters used in this paper as

$$N_{\rm OB,KS} \approx 550\, n_{g0}^{1.4} H_{100\rm pc}^{1.4} R_{\rm d,kpc}^{2} \tau_{\rm OB,30}. \quad (24)$$

An important point to note is that the scaling of $N_{\rm OB,\,KS}$ with gas density is somewhat *shallower* than the scaling for the critical curve (equation 22), but comparable in magnitude (this depends on the assumed scale height and disc radius). In the case of starbursts, the normalization for the KS relation can be larger (Kennicutt & Evans 2012), but this normalization is also consistent with the critical curve in this paper. Also note that the critical number of OB stars (equation 22) depends sensitively on the ISM temperature and can be much smaller for a cooler (say 100 K) disc. Therefore, a comparison of equations (22) and (24) should be made only after using appropriate disc/ISM parameters. A steeper slope for critical $N_{\rm OB}$ as compared to the KS relation (despite the dependence on other parameters as disc radius and ISM temperature) implies that SNe can disrupt the star-forming regions more easily in weak/moderate star-forming regions but not in dense starbursts. This may explain the observed higher efficiency of star formation (or a larger normalization of KS relation; equation 23) in starbursts relative to moderate star-forming regions. The key uncertain step in this argument (which is beyond the scope of this paper) is how the maintenance of an overpressured bubble translates into suppression of star formation.

We can also compare our critical $N_{\rm OB} - n_{g0}$ curve with the observed threshold of SFR $\sim$0.1 $\rm M_\odot\ yr^{-1}\ kpc^{-2}$ for galactic superwinds (e.g. Heckman 2002). Using similar arguments used to derive equation (24), the critical SFR density corresponding to our critical curve is

$$\Sigma_{\rm SFR,crit} \sim 2\times10^{-4}\,{\rm M_\odot\ yr^{-1}\ kpc^{-2}} n_{g0}^{1.89} R_{\rm d,kpc}^{-2}. \quad (25)$$

While this is much smaller than the Heckman limit, it is comparable to the lower limit on SFR density for the appearance of radio haloes in spiral discs, $\sim10^{-4}$ erg cm^{-2}s^{-1} (equivalent to SFR density of $10^{-5}\,\rm M_\odot\ yr^{-1}\ kpc^{-2}$; Dahlem, Lisenfeld & Golla 1995). Roy et al. (2013) argue that to form a galactic superwind the superbubble has to break out with a sufficiently high Mach number ($\gtrsim 5$), but our critical curve (equation 21) is based on a Mach number of unity.

4.2 Radius–velocity distribution of H I supershells

Our setup provides an opportunity to study the observed properties of H I shells supershells, especially the ones which are close to spherical and not much affected by the background density stratification. Fig. 16 compares the radius–velocity distribution of observed H I supershells (Heiles 1979; Bagetakos et al. 2011; Suad et al. 2014) with the evolution seen in our numerical simulations; also shown are the Castor et al. (1975) analytic scalings. We can write the radius and velocity of the shell in terms of the parameter $L_{\rm w,38}/n_{g0}$ (luminosity $L_{\rm w,38} \approx N_{\rm OB,\,2} E_{SN,\,51}/\tau_{\rm OB,\,30}$ is the mechanical luminosity scaled to 10^{38} erg s^{-1}) using equation (11) as

$$\frac{L_{\rm w,38}}{n_{g0}} = \left(\frac{r_{\rm sb}}{58\ \rm pc}\right)^2 \left(\frac{v_{\rm sb}}{34\ \rm km\ s^{-1}}\right)^3. \quad (26)$$

The vertical colour bar in Fig. 16 shows the contours of constant L/n_{g0}. The '□' symbols represent the radius and velocity obtained from our simulations ($N_{\rm OB}/n_{g0}$ ranges from 100 to 10^5); it is very encouraging that the observed distribution of $r_{\rm sb} - v_{\rm sb}$ is similar to our simulations, which correspond to reasonable star-cluster parameters. The solid red colour track marks the evolution of a bubble with $N_{\rm OB} \approx 10^3$ and $n_{g0} = 1.0$ cm^{-3}, which corresponds to $L_{\rm w,38}/n_{g0} \approx 10$. But the track lies close to the analytic contours of

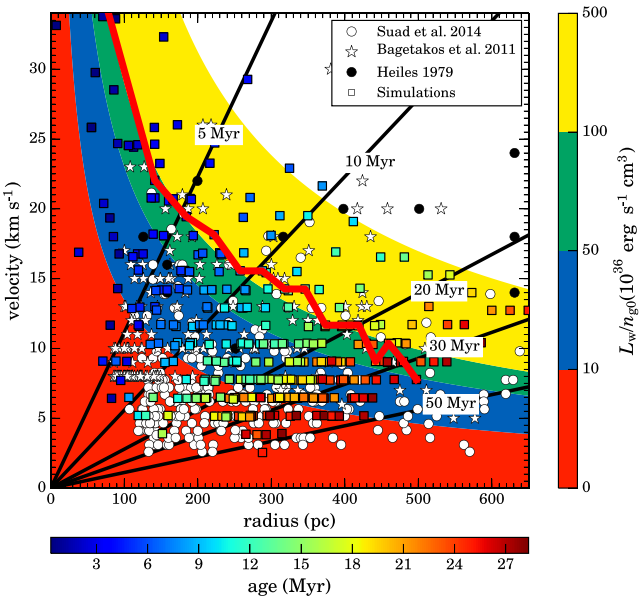

Figure 16. Radius–velocity distribution of supershells from analytic estimates (vertical colour bar; $\eta_{\rm mech} = 1$ is used in equation 10), our numerical simulations (coloured squares; horizontal colour bar indicates time), and observations (black and white symbols; Heiles 1979; Bagetakos et al. 2011; Suad et al. 2014) of H I supershells. The radius from simulations corresponds to the inner radius in spherically averaged density profiles ($R_{\rm I}$) of the shell and the velocity is obtained by $dR_{\rm I}/dt$. Solid black lines correspond to the dynamical age ($1.67 r_{\rm sb}/v_{\rm sb}$; see equations 9 and 10). The solid red line shows the evolution of velocity and radius for $N_{\rm OB} = 1000$, $n_{g0} = 1$ cm^{-3}, $r_{\rm cl} = 100$ pc. At early times, the line closely follows the analytic curve for $L_w/n_{g0} = 10^{38}$ erg s^{-1} (corresponding to $N_{\rm OB} = 100$ and $n_{g0} = 1$ cm^{-3}), with a factor of $\sim$10 smaller mechanical luminosity; at later times it dips even further. This is consistent with the radiative efficiency of $\lesssim$10 per cent, which decreases with time (Fig. 14).

$L_{\rm w,38}/n_{g0} \approx$ 0.5–1.0. It means that for a given $r_{\rm sb} - v_{\rm sb}$ the adiabatic theory overestimates $L_{\rm w,38}/n_{g0}$ by a factor of $\sim$ 10–20. This discrepancy is primarily due to large radiative losses; mechanical efficiency in Fig. 14 $\lesssim$ 10 per cent is consistent with the evolution in the $r_{\rm sb} - v_{\rm sb}$ space. Also we note that some of the simulation points (below the $t = 30$ Myr line) have a dynamical age ($\equiv 5r_{\rm sb}/3v_{\rm sb}$) longer than the simulation time.

If SNe are the dominant cause of bubble formation, then we require large OB associations for the creation of the observed H I supershells. In order to quantify the size of OB associations, we also need to evaluate the mechanical energy injection from stellar winds and radiation. However, even without accounting for these additional energy/momentum sources, the observed shells are much smaller and slower compared to what is expected from the predictions of adiabatic theory applied to the observed stellar population—the so-called power problem in superbubbles (Oey 2009 and references therein). Our simulations show that radiative losses can account for the power problem.

4.3 Gas removal from clusters

Due to the presence of feedback from OB stars (radiative, stellar winds and SNe), the star-forming regions clear gas on time-scales $\sim10^6$ yr (Lada & Lada 2003). For clusters simulated by us the $m_{\rm stars}/m_{\rm cl} \sim 0.17 N_{\rm OB,2}/n_{g0} r_{\rm cl,100}^3 < 1$ (for each OB star, the total stellar mass is $\sim$100 $\rm M_\odot$ for Kroupa/Chabrier initial mass function), therefore the gravitational well is largely provided by the

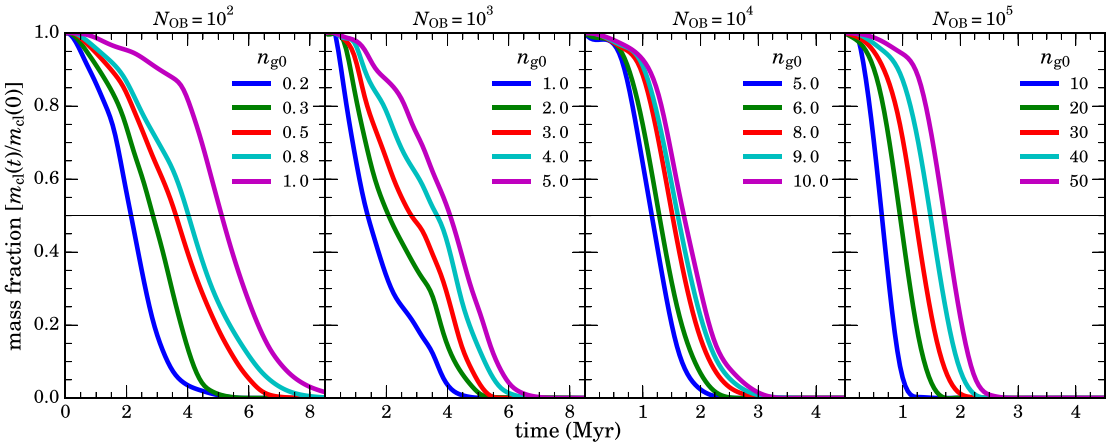

Figure 17. The fraction of original cluster gas remaining within the cluster ($r < r_{cl}$; $r_{cl} = 100$ pc for all these runs) as a function of time for various SN counts (N_{OB}). Each of the sub-panels shows curves corresponding to different values of gas density n_{g0}, the initial ISM density inside the cluster. It is noted that even a small N_{OB} makes the cluster lose all its gas by about 8–10 Myr. The evacuation time increases with density, as expected.

cluster gas (this is also true for embedded clusters buried in their natal molecular clumps.). As a result of gas expulsion, the cluster potential becomes shallower and the cluster may become unbound depending on the ratio of gas removal time-scale and dynamical time-scale of the cluster (Lada & Lada 2003). If the gas expulsion time is long compared to the dynamical time, the stars can adiabatically attain new viral equilibrium without being unbound. However, in the opposite regime because of a suddenly reduced gravity majority of stars become unbound. The time-scale of gas expulsion is also important to account for multiple populations observed in globular clusters (e.g. Krause et al. 2016 and references therein).

While our simulations do not account for gravity that holds the star cluster together (inclusion of gravity is important for strongly bound massive clouds, not so much for smaller clumps with lower gravitational binding energies), we can qualitatively understand the action of SN/stellar wind energy injection in gas expulsion from star clusters. Fig. 17 shows the mass fraction $m_{cl}(t)/m_{cl}(0)$ (m_{cl} is the gas mass inside the cluster radius, $r < r_{cl}$) as a function of time for various values of N_{OB} and n_{g0}. Since the ratio of energy injected by SNe to the gravitational potential energy $\sim N_{OB} E_{SN}/(G\mu^2 m_p^2 n_{g0}^2 r_{cl}^5) \sim 5 \times 10^5 N_{OB,2} E_{SN,51}/(n_{g0}^2 r_{cl,2}^5)$ is large, the effect of neglecting gravity is negligible for the choice of our parameters (for simulations with gravity, see Calura et al. 2015; Krause et al. 2016). We find that the clusters are evacuated due to the formation of a superbubble within $\lesssim$10 Myr (Fig. 17). As expected, lower ISM density and higher N_{OB} evacuate the cluster gas in a shorter time. An estimate of evacuation time-scale is given in equation (16). The estimate depends strongly on the cluster radius (r_{cl}) but is weakly sensitive to parameters such as ISM density, N_{OB}, η_{mech}, etc. The results in Fig. 17 are consistent with the time-scale in equation (16); therefore, for different parameters our numerical results can be scaled according to the theoretical scaling.

4.4 Convergence of η_{mech} and temperature distribution of radiative losses

One of the key questions is whether our results are converged. Convergence of the fiducial 3D simulation is discussed in Appendix B. Fig. B1 clearly shows that the higher resolution simulations show finer features. What about the convergence of volume-averaged quantities such as mechanical efficiency (η_{mech})? Fig. 18 shows mechanical efficiency (equation 19) measured at 30 Myr for the

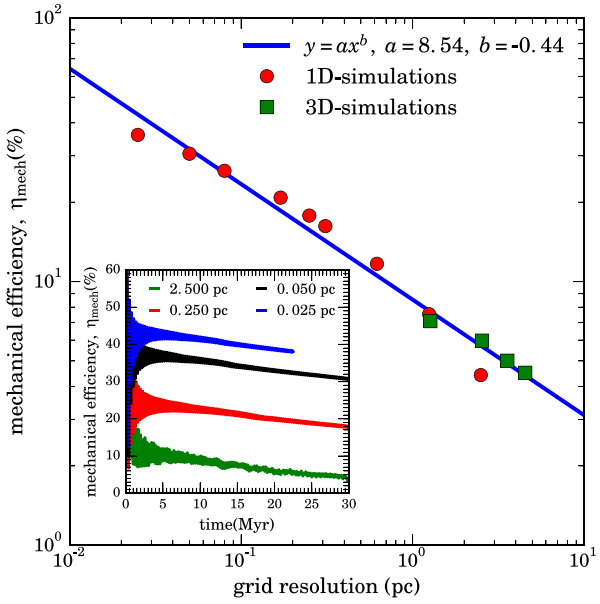

Figure 18. Mechanical efficiency measured at 30 Myr as a function of grid resolution for various 1D and 3D superbubble simulations. The grid parameters are $N_{OB} = 100$, $n_{g0} = 1$ cm^{-3} and $r_{cl} = 0$ (for 1D runs) and $r_{cl} = 100$ pc (for 3D runs). The blue solid line is the best least squares power-law fit to the data points. The inset shows the evolution of mechanical efficiency for the high-resolution 1D runs. Mechanical efficiency does not converge even for the highest resolution 1D simulations.

fiducial 3D and 1D runs at various resolutions. Even average quantities like η_{mech} do not show perfect convergence (we get a higher value of η_{mech} with increasing resolution.). The 1D simulations can be carried out at a much higher resolution than the 3D ones, and yet η_{mech} increases with an increasing resolution. In Section 3.3, we show that at the same resolution the radiative losses are comparable in 3D and 1D (top-right panel of Fig. 9). From this, we expect that even the very high resolution 3D simulations (which are beyond the capabilities of current computational resources) will not show convergence.

Recent, very high-resolution 1D simulations (Gentry et al. 2016; Gupta et al. 2016) have highlighted the importance of very high resolution to obtain mechanical efficiency and momentum delivered

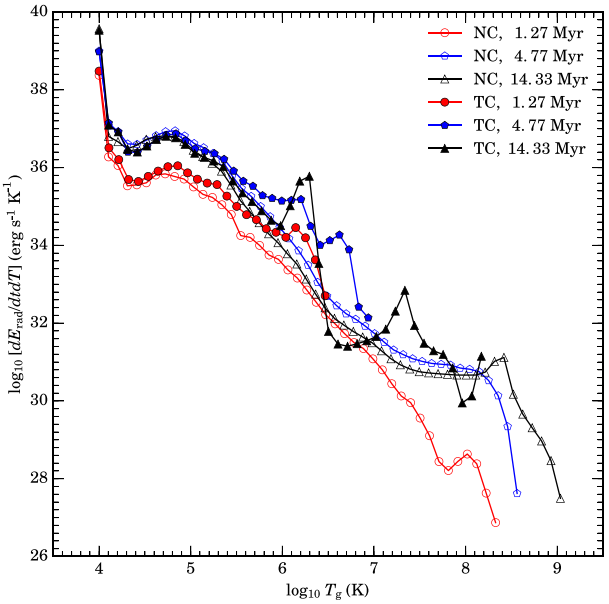

Figure 19. Radiative loss rate per temperature bin ($dE_{\rm rad}/dtdT$) as a function of gas temperature at different times for our fiducial simulation with (TC) and without (NC) thermal conduction. We calculate the radiative loss rates in logarithmically spaced temperature bins with $\Delta\log_{10}T = 0.1$. Thermal conduction reduces the maximum gas temperature in the box because of evaporation of matter into the hot bubble.

to the ISM by SNe. However, our Fig. 18 clearly shows the lack of convergence even at the highest resolutions. The cooling losses in any simulation with unresolved boundary layers (radiative relaxation layer and contact discontinuity) will keep on decreasing with an increasing resolution because the volume of cooling layers (and hence radiative loss rate) decreases with an increasing resolution. This means that convergence can only be achieved by explicitly including diffusive processes such as thermal conduction and/or viscosity, which can numerically resolve the radiative layers. Moreover, the values of physical conductivity and viscosity are too small (especially for the dense phases) to be resolved on the grid. Therefore, artificially large numerical diffusivities (which may crudely mimic small-scale turbulent transport) must be used. The importance of resolving cooling layers via explicit thermal conduction to obtain convergence in thermal instability simulations is highlighted in Koyama & Inutsuka (2004). Similarly, Fromang & Papaloizou (2007) and Lesur & Longaretti (2007) show that explicit resistivity and viscosity are required to get converged results for angular momentum transport due to magnetorotational instability (MRI) in unstratified shearing boxes.

One observationally important diagnostic is the temperature distribution of cooling losses in superbubbles; this determines the wavebands in which they emit. Fig. 19 shows the temperature distribution of the radiative loss rate for the fiducial 3D run with and without thermal conduction. Both with and without conduction, the radiative losses occur primarily at $\sim 10^4$ K; the fractional radiative losses for $T < 10^5$ K are 99.6 per cent and 99.3 per cent with and without conduction, respectively. This result is consistent with the recent superbubble simulations in dense molecular gas (Gupta et al. 2016), which shows that the cooling losses at $\sim 10^4$ K are about two order of magnitude larger than X-ray ($\sim 10^{6-7}$ K) and molecular ($\sim$100 K) losses. Thermal conduction reduces the maximum temperature in the hot bubble due to the evaporation of mass from the dense shell to the hot bubble, as shown in Fig. 8.

5 CONCLUSIONS

We have carried out 3D hydrodynamic simulations of SNe in an OB association that creates and drives a superbubble. Our aim has been to study the effect of multiple SNe distributed over a limited region of a cluster, on the ambient material far outside the cluster, and derive the dependence of fundamental parameters such as the efficiency of energy deposition and the critical number of SN required to create overpressured bubbles. Our settings have been admittedly, and intentionally, kept idealized so that we can perform controlled numerical experiments. Physical effects such as magnetic fields, thermal conduction, stratification, and inhomogeneities in the ambient gas, which we have not included here, presumably do play important roles in superbubble formation and evolution, and will be the focus of our future studies.

The broad astrophysical implications of our results are discussed in Section 4. Our key results can be summarized as follows.

(i) While isolated SNe fizzle out by $\sim$1 Myr due to radiation losses, for a realistic cluster size it is likely that subsequent SNe go off in a hot and tenuous medium and sustain a shock lasting for the cluster lifetime $\sim$30 Myr, comparable to the galactic dynamical time-scale. 1D numerical simulations faithfully capture the global energetics but cannot, by construction, capture morphological features such as the crinkling of the contact discontinuity seen in 3D.

(ii) While most of the input energy is lost via radiative cooling, the superbubble retains a fraction $\eta_{\rm mech}$ of the input energy, and this fraction scales as $\eta_{\rm mech} \propto n_{g0}^{-2/3}$, being of the order of $\sim$6 per cent for $n_{g0} \sim 1$ cm^{-3} over a time period of $\sim$30 Myr. We note that the mechanical efficiency increases with an increasing resolution, and that converged result can only be obtained by resolving cooling layers using explicit diffusion.

(iii) We have explored the parameter space of ISM density (n_{g0}), number of SNe ($N_{\rm OB}$) and star-cluster radius ($r_{\rm cl}$) to study the conditions for the formation of an overpressured superbubble. For realistic cluster sizes, we find that the bubble remains overpressured only if, for a given n_{g0}, $N_{\rm OB}$ is larger than a threshold value. Our results show that threshold condition can be roughly expressed as $N_{\rm OB,crit} \sim 200 n_{g0}^{1.9}$, where n_{g0} is the particle density in cm^{-3}.

(iv) Classical adiabatic superbubble evolution overestimates the ratio of the wind luminosity and the ISM density ($L_{\rm w}/n_{g0}$) by a factor of $\sim$ 10–20, by not taking radiation losses into account. This explains the 'power problem' of the observed size and speed of superbubbles, and our simulations confirm that radiative losses are the reason for discrepancies between the size–speed distribution of H I supershells and the sizes of OB associations driving them.

(v) We confirm that a minimum value of $N_{\rm OB}(\gtrsim 10^4)$ is needed to produce a steady wind and a strong termination shock within the cluster region. For a smaller number of SNe, all the SN energy is deposited at the radiative dense shell.

ACKNOWLEDGEMENTS

We are grateful to the Supercomputing Education and Research Centre (SERC) at IISc for facilitating our use of Cray XC40-SahasraT cluster, without which these challenging simulations could not be carried out. This work is partly supported by the DST-India grant no. Sr/S2/HEP-048/2012 and an India–Israel joint research grant (6-10/2014[IC]; which also supports Naveen Yadav). We wish to thank Kartick Sarkar, Arpita Roy, Deovrat Prasad, Prakriti Pal Choudhury, and Prasun Dhang for many

helpful discussions. We thank Siddhartha Gupta for convincing us to study the convergence of mechanical efficiency in 1D.

REFERENCES

Alexiades V., Amiez G., Gremaud P.-A., 1996, Communications in Numerical Methods in Engineering, Vol. 12, John Wiley & Sons, Ltd., p. 31
Avedisova V. S., 1972, SvA, 15, 708
Kennicutt Jr, R. C., Bagetakos I., Brinks E., Walter F., de Blok W. J. G., Usero A., Leroy A. K., Rich J. W., 2011, AJ, 141, 23
Bigiel F., Leroy A., Walter F., Brinks E., de Blok W. J. G., Madore B., Thornley M. D., 2008, AJ, 136, 2846
Calura F., Few C. G., Romano D., D'Ercole A., 2015, ApJ, 814, L14
Castor J., McCray R., Weaver R., 1975, ApJ, 200, L107
Chabrier G., 2003, PASP, 115, 763
Chevalier R. A., Clegg A. W., 1985, Nature, 317, 44 (CC85)
Chu Y.-H., Gruendl R. A., 2008, in Beuther H., Linz H., Henning T., eds, Astronomical Society of the Pacific Conference Series Vol. 387, Massive Star Formation: Observations Confront Theory. Astron. Soc. Pac., San Francisco, p. 415
Courant R., Friedrichs K., Lewy H., 1928, Math. Ann., 100, 32
Cox D. P., 1972, ApJ, 178, 159
Creasey P., Theuns T., Bower R. G., 2013, MNRAS, 429, 1922
Dahlem M., Lisenfeld U., Golla G., 1995, ApJ, 444, 119
De Avillez M. A., Breitschwerdt D., 2005, A&A, 436, 585
Durier F., Dalla Vecchia C., 2012, MNRAS, 419, 465
Efstathiou G., 2000, MNRAS, 317, 697
Ferrand G., Marcowith A., 2010, A&A, 510, A101
Fromang S., Papaloizou J., 2007, A&A, 476, 1113
Gatto A. et al., 2015, MNRAS, 449, 1057
Gentry E. S., Krumholz M. R., Dekel A., Madau P., 2016, preprint, (arXiv:1606.01242)
Gies D. R., 1987, ApJS, 64, 545
Girichidis P. et al., 2016, MNRAS, 456, 3432
Gupta S., Nath B. B., Sharma P., Shchekinov Y., 2016, MNRAS, 462, 4532
Heckman T. M., 2002, in Mulchaey J. S., Stocke J. T., eds, Astronomical Society of the Pacific Conference Series Vol. 254, Extragalactic Gas at Low Redshift. Astron. Soc. Pac., San Francisco, p. 292
Heiles C., 1979, ApJ, 229, 533
Hennebelle P., Iffrig O., 2014, A&A, 570, A81
Joung M. K. R., Mac Low M.-M., 2006, ApJ, 653, 1266
Kauffmann G. et al., 2003, MNRAS, 341, 54
Kennicutt R. C., Jr1998, ApJ, 498, 541
Kennicutt R. C., Evans N. J., 2012, ARA&A, 50, 531
Kim C.-G., Ostriker E. C., 2015, ApJ, 802, 99
Koyama H., Inutsuka S.-i., 2004, ApJ, 602, L25
Krause M., Fierlinger K., Diehl R., Burkert A., Voss R., Ziegler U., 2013, A&A, 550, A49
Krause M., Diehl R., Böhringer H., Freyberg M., Lubos D., 2014, A&A, 566, A94
Krause M. G. H., Charbonnel C., Bastian N., Diehl R., 2016, A&A, 587, A53
Kroupa P., 2002, Science, 295, 82
Krumholz M. R., Tan J. C., 2007, ApJ, 654, 304
Krumholz M. R. et al., 2014, Protostars and Planets VI. University of Arizona Press, Tucson, p. 243
Lada C. J., Lada E. A., 2003, ARA&A, 41, 57
Larsen S. S., 1999, A&AS, 139, 393
Lesur G., Longaretti P.-Y., 2007, MNRAS, 378, 1471
Li M., Ostriker J. P., Cen R., Bryan G. L., Naab T., 2015, ApJ, 814, 4
McCammon D., Burrows D. N., Sanders W. T., Kraushaar W. L., 1983, ApJ, 269, 107
McCray R., Kafatos M., 1987, ApJ, 317, 190
McKee C. F., 1974, ApJ, 188, 335
Mac Low M.-M., Klessen R. S., 2004, Rev. Modern Phys., 76, 125
Mac Low M.-M., McCray R., 1988, ApJ, 324, 776
Martizzi D., Faucher-Giguère C.-A., Quataert E., 2015, MNRAS, 450, 504
Mignone A., Bodo G., Massaglia S., Matsakos T., Tesileanu O., Zanni C., Ferrari A., 2007, ApJS, 170, 228
O'Connell R. W., Gallagher J. S., III, Hunter D. A., Colley W. N., 1995, ApJ, 446, L1
Oey M. S., 2009, in Smith R. K., Snowden S. L., Kuntz K. D., eds, The Local Bubble And Beyond II, AIP Conf. Ser. Vol. 1156, Am. Inst. Phys., New York, p. 295
Pakmor R., Pfrommer C., Simpson C. M., Springel V., 2016, ApJ, 824, L30
Parizot E., Marcowith A., van der Swaluw E., Bykov A. M., Tatischeff V., 2004, A&A, 424, 747
Pikel'Ner S. B., 1968, Astrophys. Lett., 2, 97
Press W. H., Flannery B. P., Teukolsky S. A., 1986, Numerical Recipes. The Art of Scientific Computing, Cambridge Univ. Press
Roman-Duval J., Jackson J. M., Heyer M., Rathborne J., Simon R., 2010, ApJ, 723, 492
Roy A., Nath B. B., Sharma P., Shchekinov Y., 2013, MNRAS, 434, 3572
Sanders W. T., Kraushaar W. L., Nousek J. A., Fried P. M., 1977, ApJ, 217, L87
Sarkar K. C., Nath B. B., Sharma P., Shchekinov Y., 2016, ApJ, 818, L24
Schmidt M., 1959, ApJ, 129, 243
Sharma P., McCourt M., Parrish I. J., Quataert E., 2012, MNRAS, 427, 1219
Sharma P., Roy A., Nath B. B., Shchekinov Y., 2014, MNRAS, 443, 3463 (SRNS14)
Simpson C. M., Pakmor R., Marinacci F., Pfrommer C., Springel V., Glover S. C. O., Clark P. C., Smith R. J., 2016, ApJ, 827, L29
Stone J. M., Norman M. L., 1992, ApJ, 390, L17
Strickland D. K., Heckman T. M., Colbert E. J. M., Hoopes C. G., Weaver K. A., 2004, ApJ, 606, 829
Suad L. A., Caiafa C. F., Arnal E. M., Cichowolski S., 2014, A&A, 564, A116
Sutherland R. S., Dopita M. A., 1993, ApJS, 88, 253
Thornton K., Gaudlitz M., Janka H.-T., Steinmetz M., 1998, ApJ, 500, 95
Tomisaka K., Habe A., Ikeuchi S., 1981, Ap&SS, 78, 273
Toro E. F., Spruce M., Speares W., 1994, Shock Waves, 4, 25
Vasiliev E. O., Nath B. B., Shchekinov Y., 2015, MNRAS, 446, 1703
Vishniac E. T., 1983, ApJ, 274, 152
Walch S., Naab T., 2015, MNRAS, 451, 2757
Walch S. et al., 2015, MNRAS, 454, 238
Wang Q. D., 2014, in Ray A., McCray R. A., eds, IAU Symposium Vol. 296, Supernova Environmental Impacts. p. 273
Weaver R., McCray R., Castor J., Shapiro P., Moore R., 1977, ApJ, 218, 377
Wolfire M. G., Hollenbach D., McKee C. F., Tielens A. G. G. M., Bakes E. L. O., 1995, ApJ, 443, 152
Wünsch R., Palouš J., Tenorio-Tagle G., Silich S., 2007, in Elmegreen B. G., Palous J., eds, IAU Symposium Vol. 237, Triggered Star Formation in a Turbulent ISM. p. 497
Wünsch R., Tenorio-Tagle G., Palouš J., Silich S., 2008, ApJ, 683, 683
Wünsch R., Silich S., Palouš J., Tenorio-Tagle G., Muñoz-Tuñón C., 2011, ApJ, 740, 75

APPENDIX A: RADIUS DETERMINATION OF THE SHELL

For 3D simulations, the dense shell is not perfectly spherical. Some figures (e.g. Figs 7 and 16) show the evolution of the shell radius with time. Fig. A1 shows how we determine the inner and outer radii of the supershells. We construct angle-averaged radial density profiles by dividing the simulation box into spherical shells of thickness $\delta r = \delta L$, and averaging over all the grid cells contained within the shell. The inner shell radius is taken at the radius where $n_{\rm g} = 0.98 n_{\rm g0}$ and the outer shell radius has $n_{\rm g} = 1.02 n_{\rm g0}$.

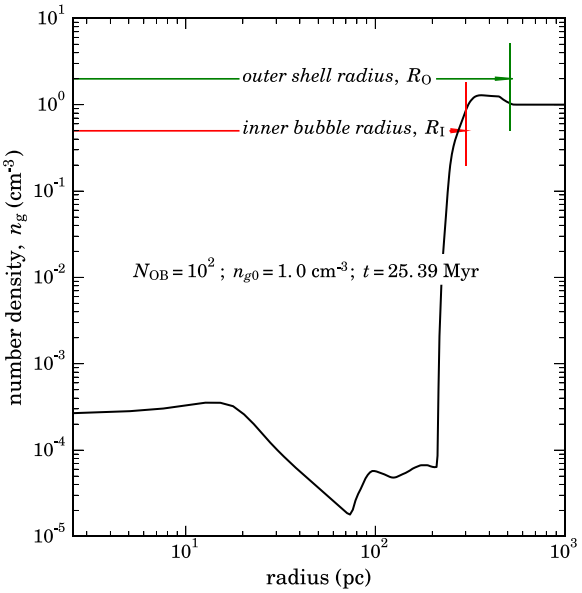

Figure A1. Determining the radius of supershells: first we calculate the angle-averaged density profiles in spherical shells of size $\delta r = \delta L$. The outer shell radius (R_O) corresponds to the radius at which the average density is larger than 1.02 times the ambient ISM density (n_{g0}) and the inner radius (R_I) corresponds to the radius at which the average density falls below $0.98 n_{g0}$.

APPENDIX B: CONVERGENCE

In order to ensure the convergence of the results, we carried out our fiducial run ($n_{g0} = 1$ cm^{-3}, $T_0 = 10^4$ K, $N_{OB} = 100$, $r_{cl} = 100$ pc) with different grid resolutions (see Table B1). The time step is shorter for a higher grid resolution as $\Delta t \propto N^{-1}$, where N is the number of grid points along any direction. Hence, the total computational cost scales $\propto N^4$, which becomes prohibitive for a large number of grid points. An optimum resolution, large enough to capture key physical features but computationally feasible, needs to be chosen.

Fig. B1 compares the evolution of volume-integrated quantities and the shell radius for various grid resolutions. A larger energy is retained and the overpressure fraction (equation 13) is larger for a higher resolution, but the difference is small for the highest resolutions ($\delta L = 1.27$, 2.54 pc). The evolution of the inner and outer shell radii is also similar.

Fig. B2 shows the density snapshots of four simulations with the grid resolution of 1.27 pc, 2.54 pc and 3.57 pc and 4.53 pc at 9.55 Myr. The simulations with higher resolution better resolve the internal structures within the bubble. Strict convergence is only expected with explicit viscosity and thermal conductivity. Since molecular transport is negligible, we do not include these in our simulations. The run with $\delta L = 2.54$ pc looks morphologically very similar to the run with $\delta L = 1.27$ pc, but is ≈16 times faster. Since simulations of the cluster over its typical lifetime (∼30 Myr) are computationally expensive, we have chosen a resolution close to $\delta L \approx 2.54$ (corresponding to run R2.5 in Table B1) for most of our simulations (see Table 1).

Table B1. Convergence runs for fiducial parameters.

Label	L (pc)	N	δL (pc)	$R_O^\dagger$ (pc)	$R_I^\dagger$ (pc)	KE (10^{51} erg)	ΔTE (10^{51} erg)	$E_{inj}^\ddagger$ (10^{51} erg)	η_{mech} (per cent)	η_O
R4.5	714	315	4.54	281	490	0.69	3.84	100.38	4.51	0.40
R3.6	714	400	3.57	293	496	0.79	4.37	103.05	5.01	0.59
R2.5	649	512	2.54	299	505	0.98	5.29	105.02	5.97	0.68
R1.3	649	1024	1.27	308	512	1.19	6.32	106.11	7.08	0.72

Notes. $^\dagger R_O$ (R_I) is the outer (inner) radius of the shell at ≈25 Myr.
‡Kinetic and thermal energy added to the simulation box by SNe.

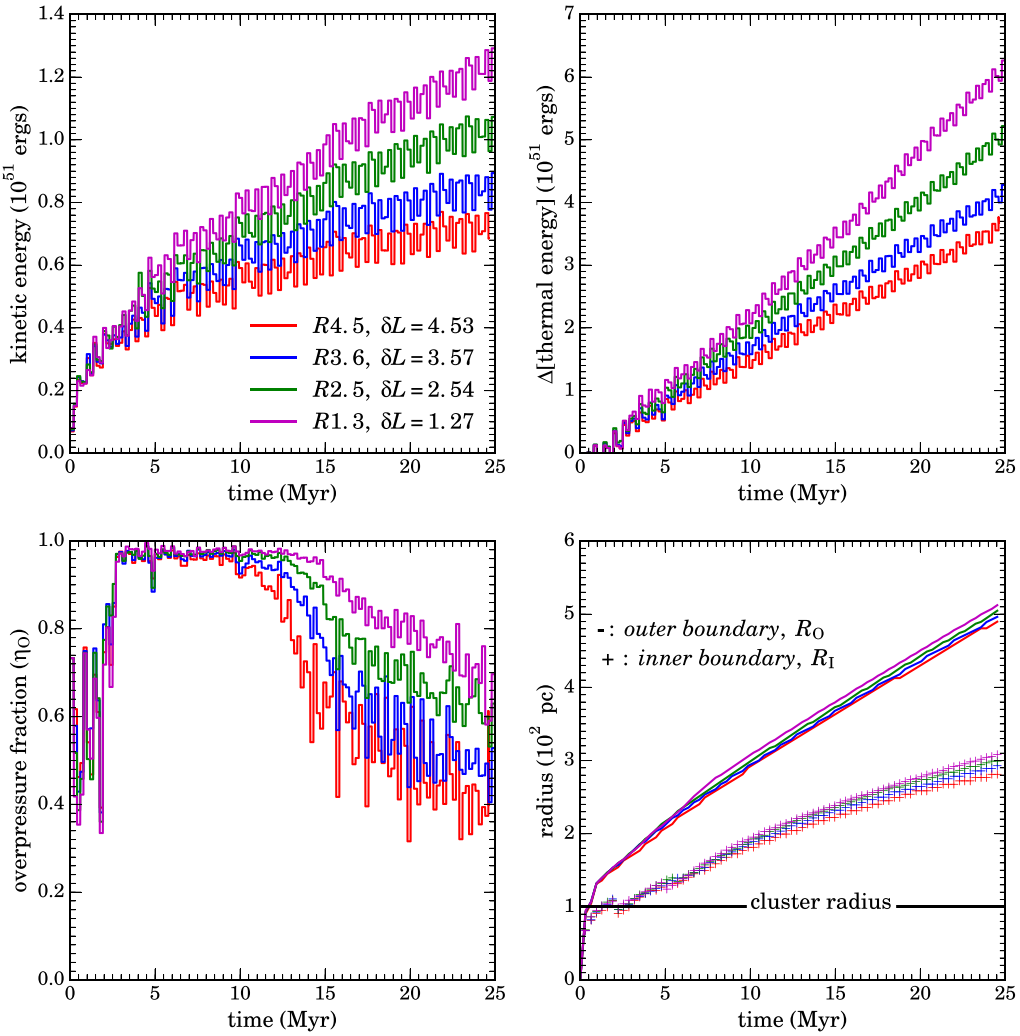

Figure B1. Various volume-averaged quantities (kinetic energy, change in thermal energy, overpressure fraction, and inner and outer radii of the shell) for the fiducial parameters ($N_{OB} = 100$, $n_g = 1$ cm^{-3}, $r_{cl} = 100$ pc) as a function of time for different grid resolutions, $\delta L = 1.27, 2.54, 3.57, 4.53$ pc. The top two and the bottom-left panels show binned data with a bin-size of 0.18 Myr. The results show convergence with an increasing resolution.

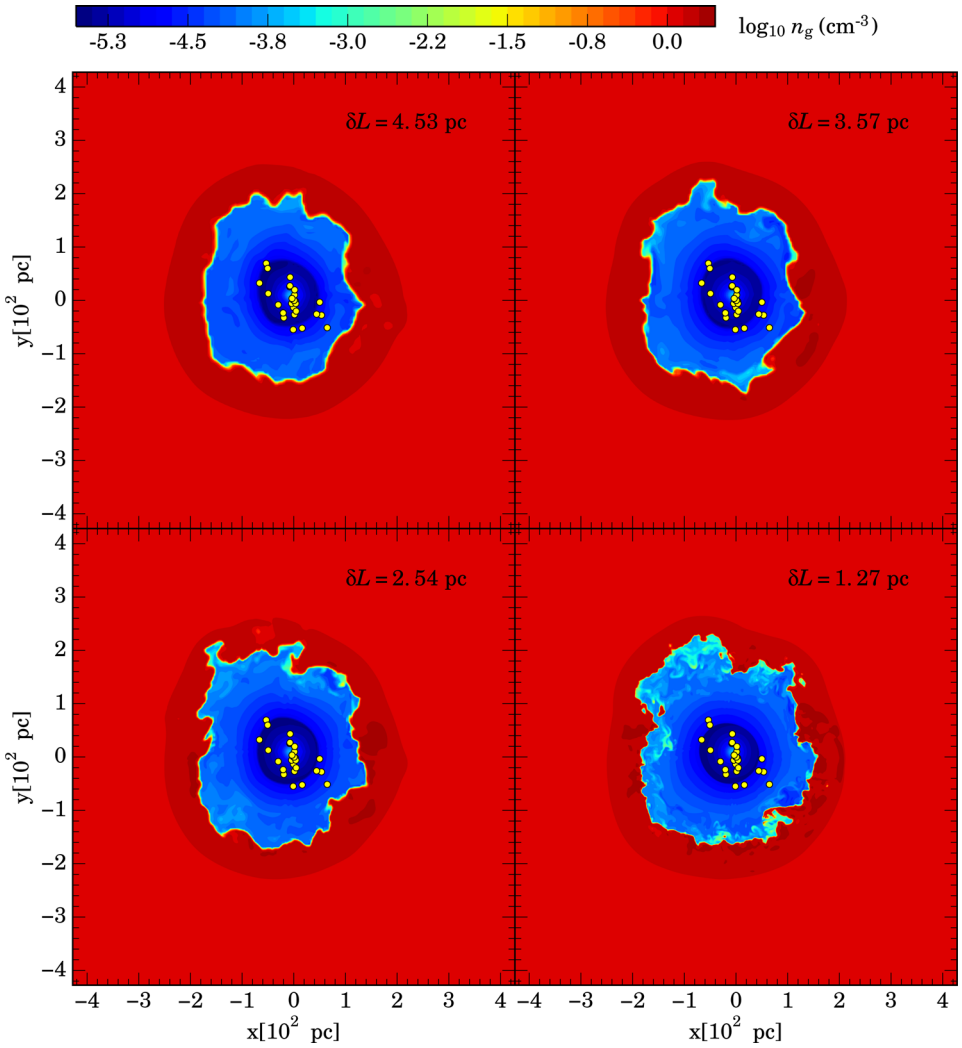

Figure B2. Density snapshots in the $x - y$ plane at 9.55 Myr for the fiducial parameters but with various grid resolutions (see Table B1). The runs with higher resolution better resolve the features at the bubble–shell interface. Yellow filled circles indicate the projected locations of SNe that have gone off.

This paper has been typeset from a TEX/LATEX file prepared by the author.